

Nano boron nitride flatland

Cite this: *Chem. Soc. Rev.*, 2014, **43**, 934

Received 17th July 2013

DOI: 10.1039/c3cs60260e

www.rsc.org/csr

Amir Pakdel,* Yoshio Bando and Dmitri Golberg*

Recent years have witnessed many breakthroughs in research on two-dimensional (2D) nanomaterials, among which is hexagonal boron nitride (h-BN), a layered material with a regular network of BN hexagons. This review provides an insight into the marvellous nano BN flatland, beginning with a concise introduction to BN and its low-dimensional nanostructures, followed by an overview of the past and current state of research on 2D BN nanostructures. A comprehensive review of the structural characteristics and synthetic routes of BN monolayers, multilayers, nanomeshes, nanowaves, nanoflakes, nanosheets and nanoribbons is presented. In addition, electronic, optical, thermal, mechanical, magnetic, piezoelectric, catalytic, ecological, biological and wetting properties, applications and research perspectives for these novel 2D nanomaterials are discussed.

1 Introduction

1.1 Basics of boron nitride

Boron nitride (BN) is a chemical compound consisting of equal numbers of boron (B) and nitrogen (N) atoms. BN is not found in nature and is therefore produced synthetically from B, boric acid (H_3BO_3) or boron trioxide (B_2O_3). The first synthesis of

World Premier International Center for Materials Nanoarchitectonics (WPI-MANA), National Institute for Materials Science (NIMS), 305-0044 Tsukuba, Japan.
E-mail: PAKDEL.Amir@nims.go.jp, GOLBERG.Dmitri@nims.go.jp; Fax: +81-29-851-6280; Tel: +81-29-860-4696



Amir Pakdel

HRTEM structural characterization, surface functionalization, spectroscopic chemical analysis and applications of various BN and BN-C nanomaterials. His current research focuses on interface engineering of hierarchical 1D and 2D BN nanostructure films to control their static and dynamic non-wetting properties.

BN was performed in 1842 by Balmain,^{1,2} using the reaction between molten H_3BO_3 and potassium cyanide (KCN). Until the early 1960s, it was not possible to stabilize this material in the form of powders and hot-pressed shapes. However, modern processing technology has made BN an economically affordable advanced material which is used in various forms.

BN is isostructural to carbon (C) and exists in various crystalline forms. The hexagonal form (h-BN) is a white slippery BN polymorph with a layered structure analogous to graphite. The layered structure can also be stacked in the rhombohedral form. The other common structure of BN is the cubic form (c-BN) which is similar to diamond and is the second



Yoshio Bando

Yoshio Bando received his PhD at Osaka University in 1975 and joined the National Institute for Research in Inorganic Materials (currently, National Institute for Materials Science, NIMS). He is now a NIMS Fellow and the Chief Operating Officer (COO) of the International Center for Materials Nanoarchitectonics (MANA). He has served as a Professor at the University of Tsukuba (1992–2008), and an Adjunct Professor at Waseda University (2008–present). He has received the 3rd Thomson Reuters Research Front Award (2012) and the 16th Tsukuba Prize (2005). His current research concentrates on the synthesis of novel inorganic nanomaterials and their TEM analysis.

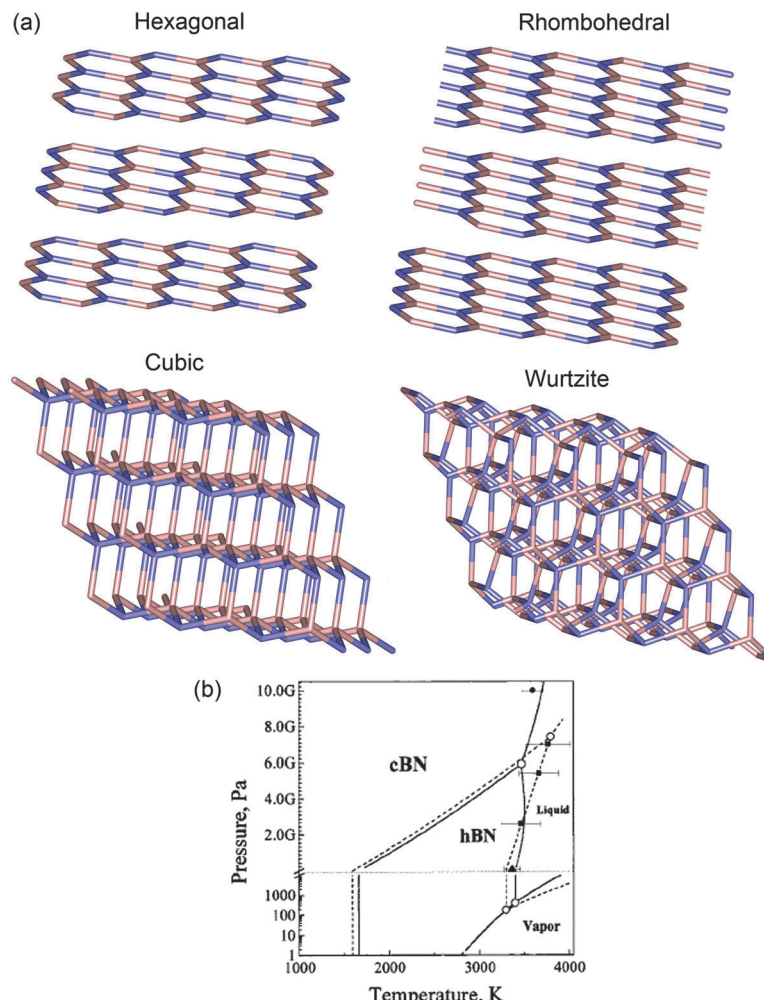


Fig. 1 (a) Boron nitride crystal structures. (b) Phase diagram of BN. Solid and dashed lines represent refined and primary diagrams. The solid circles and squares show the melting point of c-BN measured at different pressures and the solid triangle is the melting point of h-BN at 50 MPa.³

hardest material known to date. There is also a rare wurtzite form which is similar to lonsdaleite. Fig. 1 summarizes

the BN polymorphs and the corresponding equilibrium phase diagram.



Dmitri Golberg

He is currently a Unit Director and a Principal Investigator within the WPI International Center for Materials Nanoarchitectonics (MANA) of NIMS, and a Professor of the University of Tsukuba.

Dmitri Golberg obtained his PhD degree from the Institute for Ferrous Metallurgy, Moscow, Russia, in 1990, and joined the National Institute for Materials Science (NIMS), Tsukuba, Japan, five years later. In 2005 he was awarded the 16th Tsukuba Prize for his studies on inorganic nanotubes using electron microscopy, and in 2012 he became a recipient of the 3rd Thomson Reuters Research Front Award for his studies on 1D-nanomaterials.

1.2 Phase stability of boron nitride

One of the debated issues about BN is the relative stability of its main allotropes, *i.e.*, c-BN and h-BN. The former is a dense phase with sp^3 hybridized B–N bonds, while the latter is a low-density phase with sp^2 hybridized bonds. Until the early 1990s, it was believed that h-BN was thermodynamically more stable than c-BN in standard conditions (although, at high pressures the situation was reversed, similar to the graphite and diamond phases of carbon). This premise was supported by the fact that BN synthesis usually results in the formation of h-BN. However, subsequent analysis and measurements resulted in a different conclusion which is now generally accepted; namely, at zero pressure c-BN is the thermodynamically stable phase up to relatively high temperatures.^{3–5} The transformation temperature from c-BN to h-BN has been a matter of controversy for a long time. Will *et al.* demonstrated that kinetics is a decisive factor in this regard, and the “c-BN \leftrightarrow h-BN” transformation strongly depends on material parameters, such as purity, grain size, and defect concentration.

The stability of the cubic phase in BN in standard conditions is supported by most density-functional theory (DFT) studies.^{6–10} Nevertheless, there are theoretical works that estimate h-BN to be more stable than c-BN based on generalized gradient approximation (GGA) and local-density approximation (LDA) calculations.^{11–13} Recently, it was suggested that the intrinsic deficiencies of the DFT method become critical for the small energy differences involved in the BN system, which renders this method incapable of providing a fully consistent and conclusive picture. Instead, the application of periodic local Møller-Plesset second-order perturbation theory (MP2) reverts the order of the relative stability and favours the cubic phase. This indicates that long-range electron correlation is decisive for the relative stability of the BN polymorphs, thus the physically correct description of dispersion is crucial for evaluating this quantity.¹⁴

1.3 Nanomorphologies of boron nitride

The identification of carbon nanotubes in 1991¹⁵ encouraged extensive theoretical and experimental studies on other 1D nanostructures based on similar honeycomb-like networks. Layered BN (h-BN) was one of these materials. The successful synthesis of pure BN nanotubes was first reported in 1995.¹⁶ Other 1D BN nanomaterials such as nanowires, nanofibers and nanorods were subsequently synthesized.^{17–19} Also, inspired by C₆₀ buckyballs,²⁰ the first effectual experiments on 0D nested and single-layered octahedral BN fullerene synthesis were reported in 1998.^{21,22} Afterwards, in 2004,²³ the rise of graphene and the subsequent research progress on single and multilayered graphitic nanosheets inspired curiosity about the existence and stability of their 2D BN counterparts.²⁴ A few months later, h-BN nanosheets were initially prepared in the form of so-called nanomeshes,²⁵ and a year after that, free-standing 2D BN flakes were peeled off BN crystals.²⁶ In addition, BN nanoribbons,

defined as nanosheets with variable lengths but narrow widths, were originally produced as hollow nanostrips in 2008.²⁷ Structural models of 0D, 1D and 2D BN nanostructures are illustrated in Fig. 2. Today, eighteen years after the initial synthesis of BN nanotubes, research on the lightest Group III–V compound has developed far enough to establish BN nanostructures as one of the most promising non-carbon nanosystems. Among the various nanomorphologies of BN, nanosheets and nanoribbons have been selected for discussion in the following sections of the present review.

2 Structural characteristics

An h-BN layer may be depicted as a graphene layer, in which the C atoms have been fully substituted by alternating B and N atoms. Analogous to graphene, within each h-BN layer, the atoms are bound together by strong covalent bonds, while there are weak van der Waals forces between the layers. The crystallographic parameters of h-BN and graphite are almost identical, as summarized in Table 1.²⁸

2.1 Theoretical aspects

Unlike the popular graphene monolayers, their corresponding BN sisters have rarely been observed due to the peculiar stacking characteristics of B–N. The hexagons of neighbouring planes in h-BN are superposed, *i.e.*, B and N atoms are in succession

Table 1 Crystallographic information for h-BN and graphite

Material	Crystal structure	Nearest neighbor distance (nm)	Lattice parameters (nm)	Inter-layer spacing (nm)
h-BN	Hexagonal	0.144	<i>a</i> : 0.250 <i>c</i> : 0.666	0.333
Graphite	Hexagonal	0.142	<i>a</i> : 0.246 <i>c</i> : 0.670	0.335

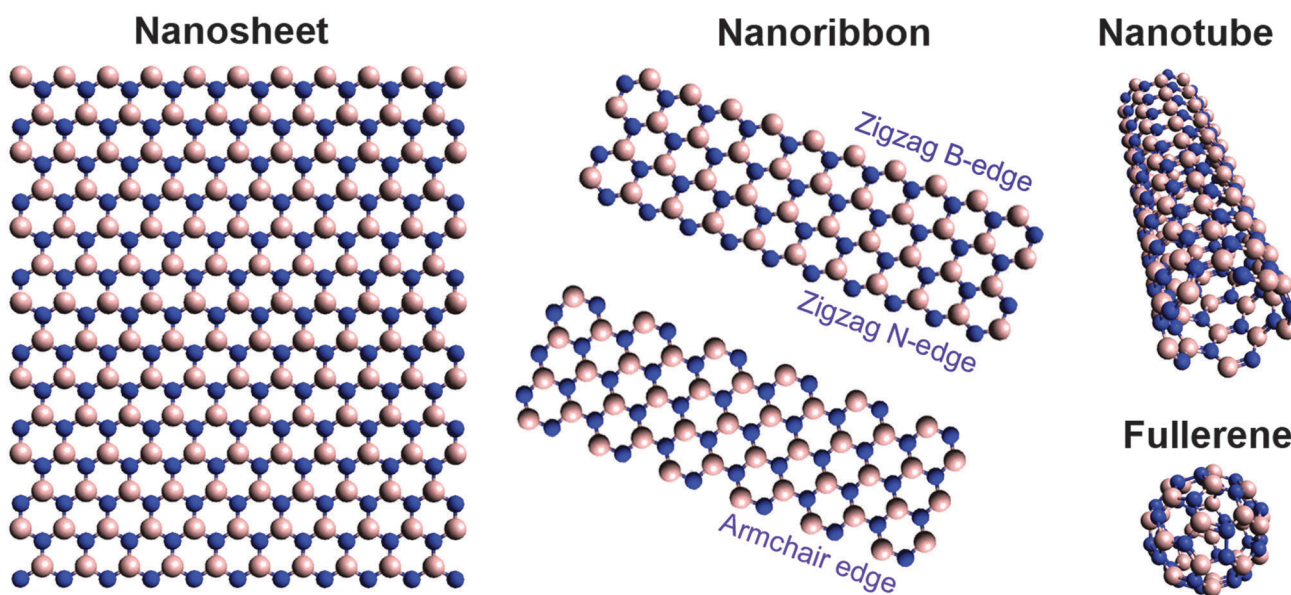


Fig. 2 Structural models of 2D, 1D and 0D BN nanostructures. The edge of a nanosheet or nanoribbon can be either zigzag (B- or N-edged) or armchair (BN pair-edged).

along the *c* axis (AA' stacking), while in graphite they are shifted by half a hexagon (AB stacking), as schematically depicted in Fig. 3(a)–(d).²⁹ *Ab initio* molecular dynamics simulations have been performed to evaluate the energy cost associated with a frustrated N–N or B–B bond as compared to a B–N bond. Starting from an isolated h-BN sheet, if two neighbouring B and N atoms are exchanged (*i.e.*, two B–B bonds and two N–N bonds are created), the computed energy cost of this antisite defect is 7.1 eV, after atomic relaxation.³⁰ Also, due to the difference in electronegativity of B and N, the B–N bonds are partially ionic, in contrast to the C–C bonds in graphitic structures. These features can lead to “lip–lip” interactions between neighbouring layers in BN nanostructures, *i.e.*, chemical bonds form as bridges or “spot-welds” between the atoms of adjacent layers. This phenomenon contributes to a metastable energy minimum by decreasing the number of dangling bonds at the edges/tips and reducing the frustration effect (*i.e.*, when B–B and N–N bonds form instead of the more energetically favourable B–N bonds). Therefore, formation of multilayered BN stabilizes the whole structure.^{30–33}

In addition, a very recent DFT study suggests that covalent interlayer B–N bonds are spontaneously formed across the adjacent BN bilayers, resulting in a structure analogous to a folded monolayered BN, as depicted in Fig. 3(e) and (f). The calculated structural relaxations result in interlayer covalent bonds forming across the bilayered zigzag edge, leading to a “closed” edge termination. The calculations predict an energy gain of –4.9 eV for each interlayer bond formed at the edge. Although these interlayer bonds in the out-of-plane direction have a covalent nature similar to the intralayer in-plane sp^2 hybridized bonds within the bulk material, the curvature at the edge leads to hybridization between σ and π symmetry states.³⁴

Moreover, van der Waals corrected DFT approach calculations suggest that the adjacent BN layers might freely slide from

AA' stacking to one of the AB stacking types (*e.g.* N centred on B–N rings on adjacent layers) along certain energetically favourable directions despite a bandgap reduction of 0.6 eV. The calculations also reveal that the main role of the van der Waals forces is to anchor the BN layers at a fixed distance, whereas the electrostatic forces dictate the optimal stacking mode and the interlayer sliding corrugation.³⁵

2.2 Experimental aspects

Transmission electron microscopy (TEM) investigations have revealed that in typical multilayered nanosheets, layers are ordered with an interlayer distance of ~0.33–0.34 nm, characteristic of the interplanar spacing in h-BN (002) planes. Fig. 4(a) shows a low magnification TEM image of the BN nanosheets prepared by a thermal CVD method.³⁶ It indicates a compact BN network consisting of very thin nanosheets that are almost transparent to the electron beam. In addition, intrinsic bending and scrolling of the nanosheets can be seen in Fig. 4(a). The dark parts are generally the cross sections of the nanosheets folded back. Fig. 4(b) is a high-resolution TEM (HRTEM) image of the BN nanosheets, in which lattice fringes can be observed with a 0.33 nm interlayer spacing. The hexagonal structure of BN can be observed in the lattice image in Fig. 4(c). The spacing between adjacent white dots is approximately 0.25 nm, corresponding to the (100) lattice constant of h-BN and the B–B or N–N atom separations in h-BN.³⁷ Therefore, the white dots correspond to the hexagonal rings rather than individual atoms. However, recent aberration corrected TEM techniques can even identify individual B and N atoms in BN nanosheets.³⁸ Fig. 4(d) and (e) show typical electron diffraction (ED) patterns of BN nanosheets. The hexagonal pattern in Fig. 4(d) manifests the six-fold symmetry of the B and N atom arrangement. The appearance of only one set of well-defined (100) diffraction spots indicates the perfect AA' registry among the different atomic layers in the

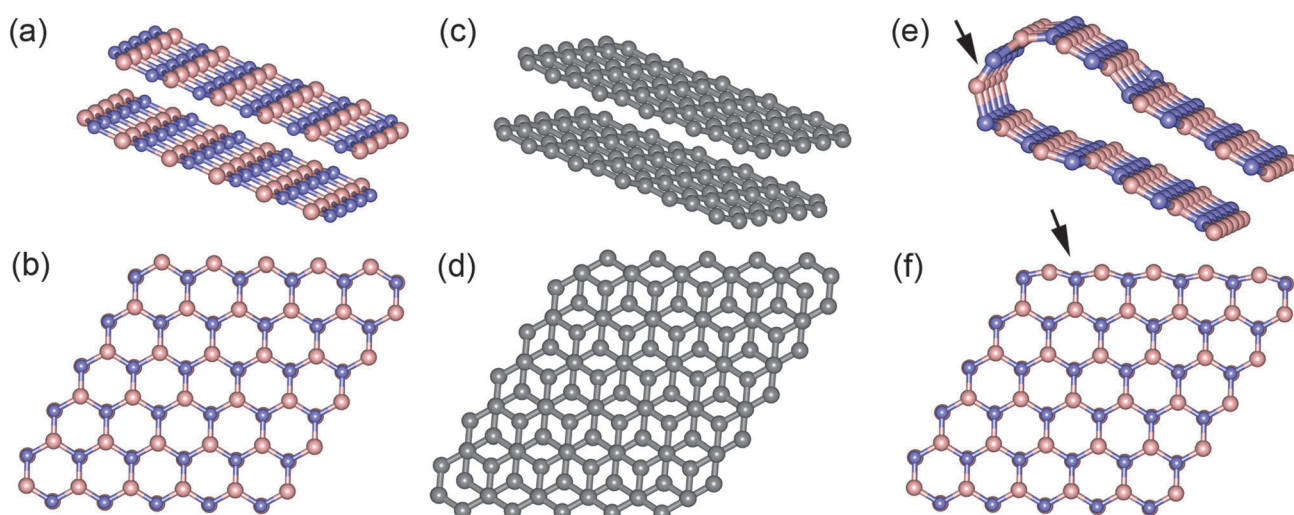


Fig. 3 Structural models of (a and b) h-BN sheets and (c and d) graphite sheets displaying the difference in their stacking sequence. Highly-crystallized graphite possesses a Bernal (AB) stacking sequence, while h-BN is stacked with the B atoms on top of the N atoms and vice versa (AA' stacking). If the discrepancy between B and N atoms is not considered, the h-BN is said to have AA stacking order. Cross-sectional and plan view of (e) the pristine and (f) relaxed models of the bilayered h-BN edge.

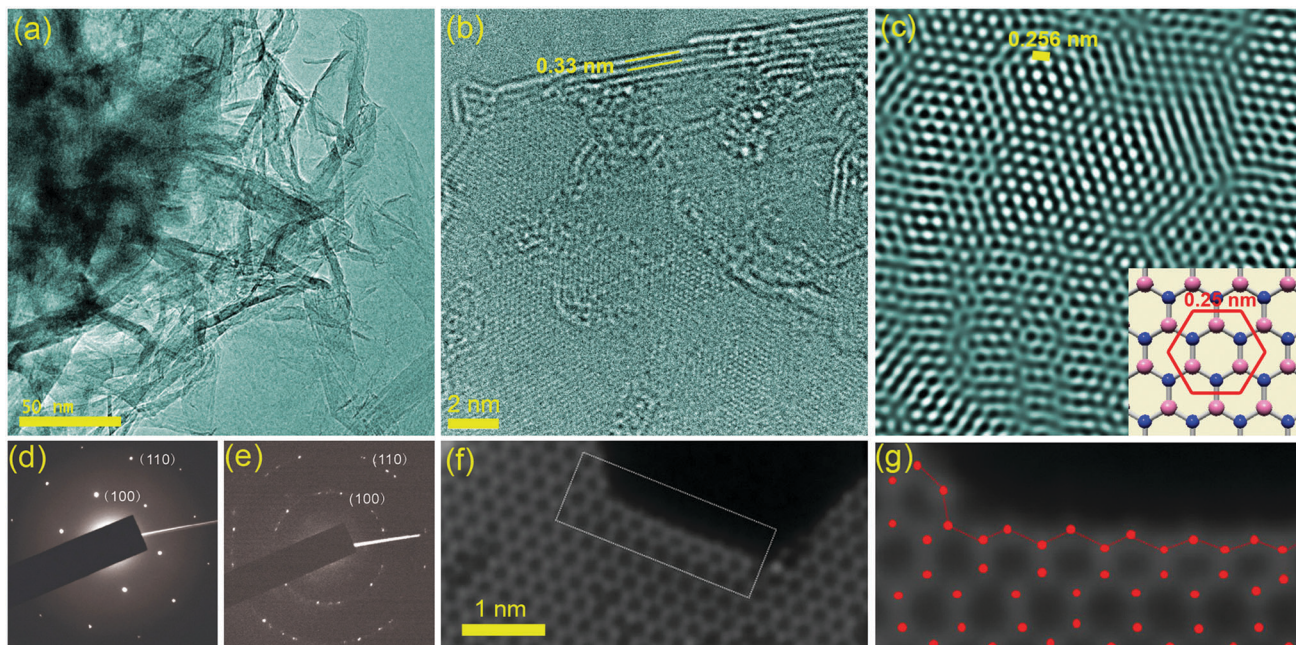


Fig. 4 (a) Low-magnification TEM and (b) HRTEM images of BN nanosheets.³⁶ (c) Lattice image of the hexagonal structure of BN.³⁷ ED patterns of BN layers displaying (d) perfect AA' registry among atomic layers and (e) rotation or disordered stacking among atomic layers.³⁹ (f) Annular dark field STEM image of a large bilayered BN sheet showing a hole with straight zigzag edges. (g) The individual atoms at the magnified BN edge (marked with red dots). A distortion pulls the zigzag edge atoms away from the hole creating a curvature at the edge.³⁴

BN sheets. However, layer rotation or disordered layer stacking among atomic layers can result in multiple sets of (100) diffraction spots appearing along the innermost circle, as displayed in Fig. 4(e).³⁹ Fig. 4(f) is an annular dark field (ADF) scanning transmission electron microscopy (STEM) image of a bilayered BN sheet. The selected area shows the formation of zigzag edges in the bilayered BN next to the hole. The higher magnification image of the region near the hole in Fig. 4(g) shows that the atoms located immediately at the edge of the membrane, marked with red dots, exhibit in-plane contraction relative to the bulk BN lattice. Such relaxation can arise from an in-plane atomic distortion due to the formation of interlayer bonds along the normal direction to the atomic planes, as displayed in Fig. 3(e) and (f).³⁴

2.3 Defect aspects

Theoretical studies on perfect nanomaterials have revealed many attractive properties; however, topological defects, vacancies, adatoms, *etc.* are inevitable in reality, significantly impacting the electronic properties and chemical reactivity of nanomaterials. In sp^2 carbon allotropes a common structural imperfection is the Stone–Wales defect, which is the rearrangement of the six-membered rings of graphene into pentagons and heptagons as a result of a 90° rotation of a C–C bond. The density of Stone–Wales defects is usually small due to the high activation barrier, several eV, for the bond rotation.⁴⁰ DFT computations on zigzag and armchair BN nanoribbons indicate that the rotation of B–N bonds to form Stone–Wales defects changes the local curvature at defect sites. This results in a small pyramidalization angle for the related atoms ($\theta_p = \theta_{\sigma\pi} - 90^\circ$) that can be used to measure their degree of sp^3 hybridization. $\theta_{\sigma\pi}$ is the angle between the σ

and π bonds, and reflects the structural deformation owing to the defect formation. Defect-free BN nanoribbons have a zero degree θ_p due to their π -conjugated planar structure. However, the B and N atoms at the heptagon–heptagon (7–7) ring fusions of Stone–Wales defects have $\theta_p > 0^\circ$, describing their degrees of sp^3 hybridization due to the formation of Stone–Wales defects. In addition, the reactions at Stone–Wales defect sites have been computed to be more exothermic than those in the centre of the perfect BN nanoribbons. The newly formed B–B and N–N bonds are the most reactive sites, followed by the pentagon–heptagon (5–7) ring fusions, irrespective of the types of ribbon edges.⁴¹ These Stone–Wales defects are thermodynamically unfavourable in h-BN layers due to the requirement for the formation of B–B or N–N bonds. However, theoretical calculations predict that such defects could be stabilized in BN nanostructures from the distortion of the nanosheet plane nearby or the formation of square–octagon (4–8) pairs.⁴²

Another structural imperfection that can influence the properties of 2D nanomaterials is the grain boundary, which is composed of aligned dislocations. Recently significant progress has been made to reveal the structures of grain boundaries and their influence on the properties of graphene and h-BN monolayers.^{43–50} In graphene, the energy of a dislocation is dominated by its elastic strain; therefore, the core of a dislocation constitutes 5–7 pairs due to their lower strain energy (compared to other polygon pairs). In h-BN however, the energy of a dislocation consists not only of topological strain but also possible homoelemental bonding (either B–B or N–N), which is weaker than the heteroelemental bonding (B–N) in a perfect lattice. 5–7 pairs have lower strain energy, but they

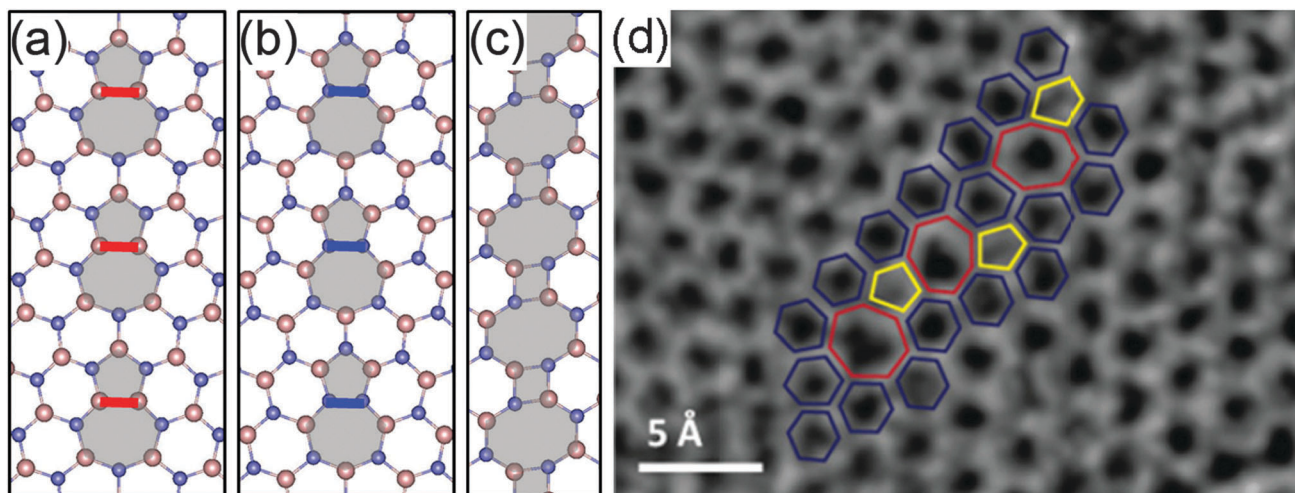


Fig. 5 Atomic models of grain boundaries: (a) polar, made of 5–7 pairs (N-rich); (b) polar, made of 5–7 pairs (B-rich); (c) nonpolar, made of 4–8 pairs.⁴⁹ (d) HRTEM image of a grain boundary in a BN film. Hexagon, heptagon and pentagon structures are depicted in blue, red and yellow, respectively.⁵⁰

inevitably introduce homoelemental bonding. On the other hand, 4–8 pairs are free of any homoelemental bonding, while suffering from higher strain energy. Theoretical calculations on the balance between the strain and chemical bonding contributions show that, depending on the tilt angle of grains, the grain boundary can be either polar (B-rich or N-rich), composed of 5–7 pairs, or nonpolar, composed of 4–8 pairs, as shown in Fig. 5(a)–(c). The polar grain boundaries carry net charges, positive at B-rich and negative at N-rich boundaries, and have a smaller bandgap compared to a perfect h-BN monolayer; in contrast to grain boundaries in graphene which generally impede the electronic transport.⁴⁹ Experimental observations of BN nanotube structures suggest that they contain 4–8 pairs,⁵¹

while very recent HRTEM images of grain boundaries in monolayered BN sheets indicate the presence of 5–7 pairs, as depicted in Fig. 5(d). The formation of 5–7 pairs in these sheets could be due to 3D wrapping along the grain boundary in the form of a wrinkle protruding normal to the lattice plane or the incorporation of C atoms into the BN lattice during synthesis.⁵⁰

Point defects have also been observed in BN mono- or bilayers under energetic electron irradiation or ion etching.^{52–54} Initially, mechanical or chemical exfoliation is used to obtain few-layered BN flakes, followed by further thinning *via* layer-by-layer sputtering processes; during which, many lattice defects such as vacancies are inevitably induced. Fig. 6(a) and (b) show HRTEM images of such defects in monolayered and bilayered BN. The discrete triangular

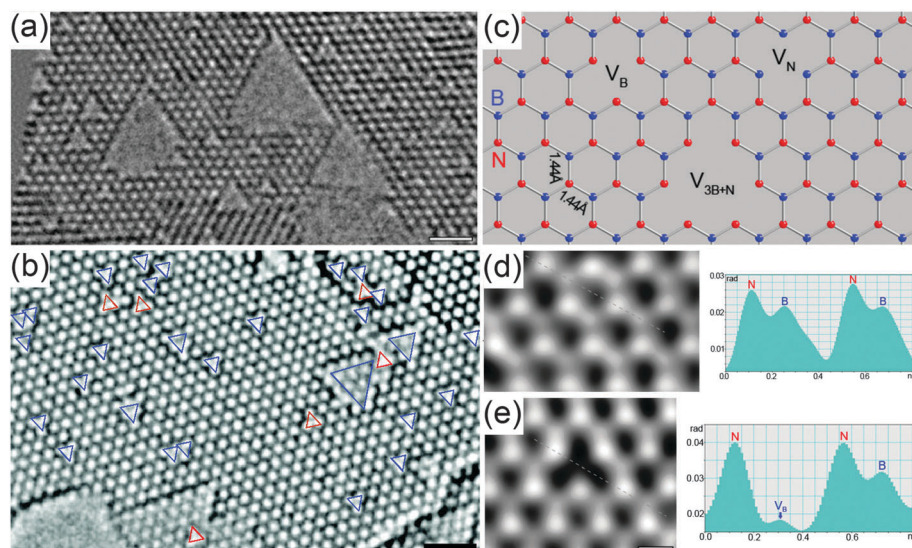


Fig. 6 (a) A typical HRTEM image showing vacancy defects in a BN monolayer, all of which are triangular with the same orientation.⁵² (b) A mostly bilayered BN membrane, in which red and blue triangles with opposite directions are vacancies in monolayered and bilayered regions, respectively.⁵³ (c) A model for the atomic defects in a BN monolayer.⁵² (d and e) Reconstructed phase images of intact and defected regions in a BN monolayer, in which the individual boron and nitrogen atoms are discriminated, and their line profiles.⁵² Scale bars in (a), (b) and (e) are 1 and 0.2 nm respectively.

holes in various sizes have been created mainly due to the knock-on effect of the incident electron beam, which is a quasielastic collision between the incident electron and the nuclei of the specimen atoms. Models for these defects are illustrated in Fig. 6(c). The smallest triangle corresponds to a monovacancy, and the larger triangles consist of several vacancies. All of these defects in the BN monolayer in Fig. 6(a) are in the same direction, while the bilayered BN in Fig. 6(b) also includes triangular defects rotated by 180°. The reconstructed phase images of intact and vacancy regions in a BN monolayer are shown in Fig. 6(d) and (e), respectively. They depict a hexagonal network of bright spots, corresponding to the individual atoms of BN. The difference in the brightness level reflects the contrast difference of the individual B and N atoms. The heavier N atoms appear in brighter contrast. A less bright atom is missing in Fig. 6(e) which can be assigned as a B monovacancy (V_B).⁵² It has been theoretically proven that B has a smaller threshold beam energy for knock-on (about 74 keV) than that of nitrogen (about 84 keV),⁵⁵ which indicates that B is removed more easily during electron beam bombardment. Therefore, all the edge-terminating atoms around the vacancies must be N. In the case of the BN bilayer in Fig. 6(b), almost all triangular defects have the same orientation on the top layer and the opposite direction on the adjacent layer. This suggests the existence of the same type of vacancy throughout the entire layered structure, considering that B atoms are above N atoms in subsequent layers of BN.⁵³

3 Synthesis

A variety of methods have been used to synthesize 2D BN nanostructures. Most of them are similar to the well-known techniques utilized for the growth of graphene sheets and ribbons with slight modifications. In this section, these methods will be discussed in detail.

3.1 Mechanical exfoliation

The pioneering procedure to obtain atomic sheets of BN was the mechanical exfoliation technique, also known as mechanical peeling or mechanical cleavage. This method was initially used to isolate graphene monolayers in 2004,²³ and a few months later, it was successfully applied to many other layered compounds such as BN, NbSe₂ and MoS₂.²⁶ In this method, layers of BN are peeled off with an adhesive tape, attached to a substrate (e.g. Si/SiO₂), and can be identified using a simple optical microscope. Nanosheets obtained with this method have a good combination of thickness and lateral size, making them suitable for fundamental studies in physics and optoelectronics.^{53,56,57} However, in contrast to the case of graphene, this technique has not been effective in rendering few-layered and monolayered BN. This may partially be due to the stronger lip-lip interactions between BN basal planes, *i.e.*, the formation of chemical bonds as bridges between the atoms of adjacent layers. This phenomenon contributes to a metastable energy minimum by decreasing the

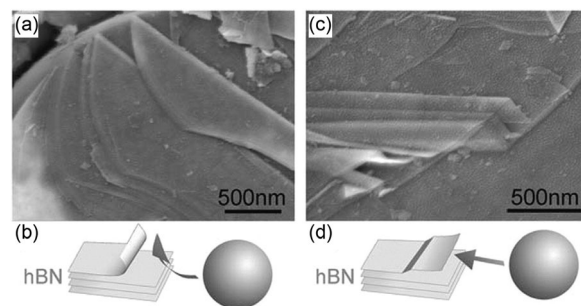


Fig. 7 (a and c) SEM images of BN nanosheets produced by a wet ball milling method.⁵⁹ (b and d) The suggested exfoliation mechanisms under the shear forces created by the milling balls.⁵⁹

number of dangling bonds at the edges; therefore, the formation of multilayered BN stabilizes the whole structure.^{31,58}

Another approach to the mechanical exfoliation of BN is the utilization of shear forces instead of direct pulling forces *via* peeling. In fact, during mechanical peeling, the pulling force easily breaks the weak van der Waals bonding between adjacent BN layers and leaves the strongly sp² bonded in-plane structure intact. A shear force can have a similar effect. In 2011, a mild wet ball-milling process was used to produce BN nanosheets from a BN powder precursor *via* gentle shear forces, under an N₂ atmosphere.⁵⁹ In this process, benzyl benzoate (C₁₄H₁₂O₂) was used as the milling agent to reduce the ball impacts and milling contamination. Fig. 7 shows SEM images of the nanosheets produced by this method and their corresponding peeling mechanisms.

3.2 Chemical exfoliation

Preparation of mono- and few-layered nanosheets from single-crystalline BN by a chemical-solution-derived method was first accomplished in 2008.⁶⁰ The transparent crystal was put in a 5 ml 1,2-dichloroethane solution of poly(*m*-phenylenevinylene-co-2,5-dicetoxy-*p*-phenylenevinylene) (1.2 mg/10 ml) and sonicated for 1 hour to disperse and break up the BN crystals into few-layered BN. To promote the BN nanosheet formation, different solvents have been employed in chemical exfoliation methods. For example, a strong polar solvent, *N,N*-dimethylformamide (DMF), was used to facilitate exfoliation due to the strong interactions between the polar DMF molecules and the BN surface. Milligram levels of pure BN nanosheets were achievable, and the majority of them had thicknesses ranging between 2 and 10 nm. The nanosheets could be dispersed in some organic solvents, such as chloroform and DMF.²⁹ In another approach, 1,2-dichloroethane was used as the solvent, which has a lower boiling point that ensures the simple and quick removal of the solvent.⁶¹

In order to obtain water-soluble BN nanosheets the precursor BN powder was functionalized with a Lewis base. Lewis bases, such as amine molecules with long lipophilic or hydrophilic chains, form complexes or adducts with the electron-deficient B atoms on BN when the mixture is heated for 4–6 days under a N₂ flow. Lewis base complexation with BN also facilitates the exfoliation of the layered structure of the bulk material. After the reaction, the extraction procedure included the addition of

the solvent to the reaction mixture, followed by brief sonication and centrifugation to separate the supernatant dispersion from the residue.⁶² In another approach, methanesulfonic acid (MSA) was used as the solvent for the liquid-phase exfoliation of BN. The precursor powder was dispersed in MSA, then the mixture was subjected to sonication for 8 hours in a low power sonic bath, followed by centrifugation for 90 min. After that, an orange supernatant was obtained. The sediments, after centrifugation, were washed with water, and collected by filtration through a pre-weighed filter. The required repulsion between adjacent layers leading to exfoliation can be due to the protonation of BN nanosheet edges and surfaces by MSA. This hypothesis is supported by the orange colour of the MSA-dispersed BN nanosheets, which can be the result of charge transfer between the acid molecules and the nanosheets.⁶³ Very recently, molten hydroxides have been used to exfoliate BN. Sodium hydroxide (NaOH), potassium hydroxide (KOH) and BN powders are ground, then transferred to a poly(tetrafluoroethylene) (PTFE)-lined stainless steel autoclave and heated at 180 °C for 2 hours. As a result, BN nanosheets and nanoscrolls are obtained, as shown in Fig. 8(a)–(c). The exfoliation process involves the following sequence: (1) self-curling of the sheets at the edges due to the adsorption of cations (Na^+ or K^+) on the outmost BN surface; (2) anions and cations entering the interlayer space and the adsorption of anions (OH^-) on the positively curved surface which drives continuous curling of the BN layer; (3) direct peeling away from the parent materials,

or cutting by the reaction of BN surface with hydroxides. This method has the advantages of being simple, one-step, low-cost, and the product can be easily transferred to any substrate by redispersion in common solvents such as water and ethanol.⁶⁴

An alternative method capable of high throughput and large-scale production of few-layered BN nanosheets is the high pressure microfluidization process. In this method, BN powder and a combination of DMF and chloroform (as the solvent) are inserted inside a microfluidizer processor and kept at a constant intensifier pump pressure of 207 MPa. This accelerates the product into the interaction chamber within which, the product stream separates into micro channels of various geometries. The stream is then forced to collide upon itself, creating incredible forces of impact and shear, which are several orders of magnitude greater than those produced by sonication. This results in exfoliation of BN with a reported yield efficiency of 45%.⁶⁵ In another method using the same concept, *i.e.*, creating shear forces *via* liquid, a small amount of BN, suspended in *N*-methyl-2-pyrrolidinone, was exfoliated inside an inclined glass tube rotating at 8000 rpm. Shearing in this case arises from the interplay between centrifugal and gravitational forces. The suspension forms in a thin layer on the inner wall of the tube at the high rotating speed. BN flakes are initially accelerated to the walls of the tube by the large centrifugal force. The liquid flow is upwards at the internal surface of the rotating tube, and downwards close to the liquid surface (Stewartson/Ekman layers). Shear layers are parallel to

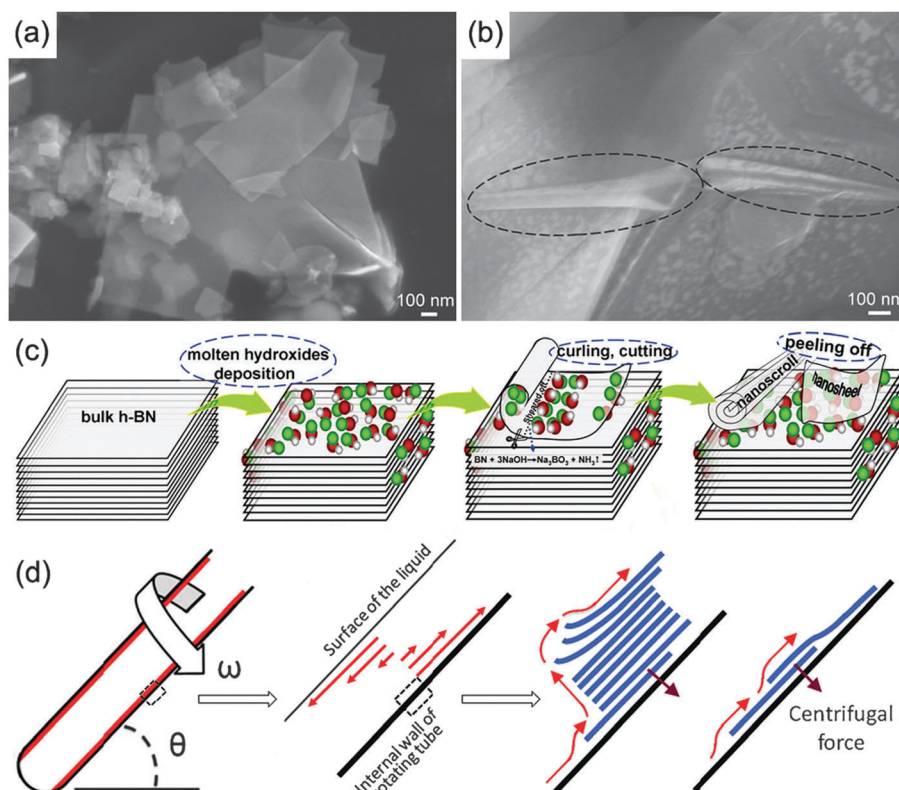


Fig. 8 (a and b) Typical flat nanosheets and curved nanoscrolls of BN.⁶⁴ (c) Illustration of the exfoliation mechanism using molten hydroxides. The green, red and white circles represent Na, O and H atoms, respectively.⁶⁴ (d) Schematic of the vortex fluidic device operating at 8000 rpm.⁶⁶

the axis of rotation and shear forces can partially lift the layers. The shear induced displacement along the tube results in layer slippage and exfoliation.⁶⁶ This process has been named “vortex fluidic exfoliation” and it is schematically illustrated in Fig. 8(d).

3.3 Chemical vapour deposition (CVD)

3.3.1 Epitaxial growth of BN monolayers. Deposition techniques have been applied to epitaxially grow BN thin films for several decades. Malcolm Basche's patent on the thermal decomposition and reaction of ammonia (NH_3) with boron trichloride (BCl_3) at 1450–2300 °C to deposit BN coatings onto a surface dates back to 1964.⁶⁷ In other early experiments, NH_3 and diborane (B_2H_6) were used as precursors for the deposition of amorphous BN thin films (less than 600 nm thick) on silicon (Si) and metallic substrates, such as tantalum (Ta), molybdenum (Mo) and germanium (Ge), in the temperature range of 600–1000 °C.⁶⁸ Current CVD growth of h-BN thin films includes the use of various chemical precursors such as $\text{BF}_3\text{-NH}_3$, $\text{BCl}_3\text{-NH}_3$, $\text{B}_2\text{H}_6\text{-NH}_3$ or the pyrolysis of a single precursor such as borazine ($\text{B}_3\text{N}_3\text{H}_6$), trichloroborazine ($\text{B}_3\text{N}_3\text{H}_3\text{Cl}_3$), or hexachloroborazine ($\text{B}_3\text{N}_3\text{Cl}_6$).^{69–75}

The first h-BN monolayer film was grown by the adsorption and decomposition of $\text{B}_3\text{N}_3\text{H}_6$ on transition metals such as Pt(111) and Ru(0001) surfaces in 1990.⁷⁶ $\text{B}_3\text{N}_3\text{H}_6$ is an analogue of benzene (C_6H_6), in which the C atoms are substituted with alternate B and N atoms in a natural B:N stoichiometry of 1:1. Therefore, chemical interaction between two or more gases (e.g. $\text{BF}_3\text{-NH}_3$ ⁷⁷ and $\text{B}_2\text{H}_6\text{-NH}_3$ ⁷⁸) is not necessary to grow the BN layers. It was proposed that borazine was completely dehydrogenated at 1000 K and the morphology of the h-BN monolayer on Pt was different from that on Ru due to the difference in interfacial bonding.⁷⁶ Theoretical calculations and experimental results have demonstrated that flat h-BN layers forming on 3d-transition metals (e.g. Ni(111)^{79–82}) and 5d-transition metals (e.g. Pt(111)⁸³) are weakly bound to the metallic substrates. However, on 4d-transition metals, the BN–substrate binding energy increases with the unoccupied states in the d-shell of the substrate.⁸⁴ For example, bonding is weaker for growth on Pd(111),⁸⁵ but stronger on Rh(111)²⁵ and Ru(0001).⁸⁶

One of the well-studied metal surfaces for forming a perfect h-BN monolayer is Ni(111). The pioneering angle-resolved ultraviolet photoelectron spectroscopy (ARUPS) investigations into the structure of valence and conduction bands of the h-BN–Ni(111) system in 1995 suggested that there was not substantial mixing of Ni d states with h-BN π states, indicating weak bonding between the metal surface and the monolayer.⁸⁷ Two years later, however, high-resolution electron energy loss spectroscopy (HREELS) studies indicated some level of hybridization between Ni d and BN π states.⁸⁸ Moreover, low-energy electron diffraction (LEED) results demonstrated that h-BN was not completely flat but slightly buckled on Ni(111) with B atoms being closer to the surface than N atoms. This buckling was attributed to the small lattice mismatch between h-BN and Ni(111), which leads to a commensurate 1 × 1 system where h-BN was slightly compressed and thus buckled.⁸⁸ This structural model was confirmed further via X-ray photoelectron diffraction

(XPD), scanning tunnelling microscopy (STM), and also theoretical studies based on DFT.^{80,81,89} Later, core level spectroscopy and near edge X-ray absorption fine structure (NEXAFS) studies demonstrated a strong hybridization between Ni-d and BN-π states, suggesting a rather strong interaction between h-BN and the metal surface.^{90,91} Further DFT studies showed that attraction/repulsion of B and N atoms toward/from the substrate depends on their position relative to the underlying metal atoms, and only when N sits on top of the metal and B occupies fcc or hcp hollow sites (Fig. 9(a)) does the B attraction dominate the N repulsion and h-BN is bound to the surface.⁸⁴

Besides Ni(111), the h-BN monolayer has been successfully formed on a number of transition metal surfaces, such as Cu(111),⁹¹ Pt(111),⁹² Pd(111),⁹³ Pd(110),⁹⁴ Fe(110),⁹⁵ Mo(110),⁹⁶ Cr(110),⁹⁷ Rh(111),²⁵ and Ru(001).⁸⁶ Among them, the h-BN/Cu(111) interface is a 1 × 1 commensurate structure as in the Ni(111) case. However its bonding is much weaker than in the h-BN/Ni(111) case, as schematically illustrated in Fig. 9(b) and (c), based on the corresponding NEXAFS and PE spectra.⁹¹ A recent study on the growth and characterization of BN layers on Cu(111) confirms that the coexistence of various Moiré patterns (resulting from a minute rotation of BN domains) together with the emergence of an electronic interface state band are due to the weak binding of the BN monolayer to Cu(111). As a result, the insulating character of bulk h-BN is preserved in these atomic layers.⁹⁸ In another approach, a low-pressure CVD (LPCVD) method was used to grow monolayer BN from $\text{NH}_3\text{-BH}_3$ on Cu substrates.⁹⁹ It was observed that unlike the hexagonal shape of graphene nucleation islands,¹⁰⁰ BN growth is in the form of triangles (Fig. 9(d)), possibly due to the more energetically favoured nitrogen-terminated edges. Besides the triangular-shaped BN monolayers at 60 °C, asymmetric diamond-shaped islands were also formed at higher sublimation temperatures (70–90 °C), as displayed in Fig. 9(e) and (f), respectively. With prolonged growth, the flakes extend in area and merge with each other resulting in a complete layer covering the Cu surface. The structure of all the other interfaces mentioned above is affected by a considerable lattice mismatch between h-BN and the metal surface, which varies between 7% and 10% depending on the substrate. For h-BN/Pt(111),⁹² Pd(111)⁹³ and Pd(110)⁹⁴ interfaces, STM images show some Moiré patterns. However, for Rh(111),²⁵ Ru(001),⁸⁶ Fe(110)⁹⁵ and Mo(110)⁹⁶ systems, well ordered nanostructures have been observed, which will be discussed in more detail in 3.3.2. To achieve high-quality 2D BN layers on transition metal substrates with minimal density of domain boundaries, low precursor pressures are required.¹⁰¹ Fig. 9(g) shows the CVD growth of BN on Ru(0001) at a low $\text{B}_3\text{N}_3\text{H}_6$ pressure. Initially, sparse arrays of BN nuclei form followed by growth to macroscopic dimensions. They then coalesce to a closed film covering the entire surface.

3.3.2 Epitaxial growth of BN nanomeshes and nanowaves.

Upon the exposure of an atomically clean Rh(111) surface to $\text{B}_3\text{H}_6\text{N}_3$ vapour at 800 °C inside an ultrahigh vacuum chamber and subsequent cooling to room temperature, a peculiar nanostructure was formed on the substrate, which was called a “BN nanomesh”.²⁵ STM observations of the product revealed a well ordered nanostructure with a periodicity of ~3 nm as

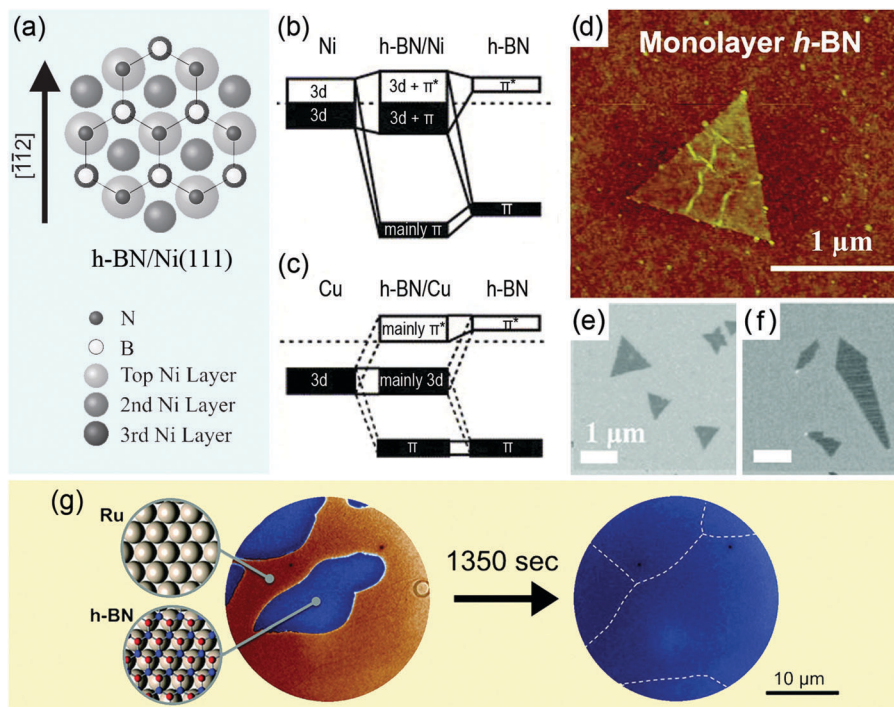


Fig. 9 (a) Top view of the h-BN/Ni(111) high-symmetry structure model. The $[1\bar{1}2]$ direction of the Ni crystal lies in the (111) surface plane.⁸⁹ (b and c) Schematic illustration of the transition metal 3d/h-BN π hybridization at the h-BN/Ni(111) and h-BN/Cu(111) interfaces, respectively. Black/white colours correspond to occupied/unoccupied states. Dotted line denotes the position of the Fermi level; strong–weak orbital mixings are shown with solid/dashed connecting lines.⁹¹ (d) AFM image of a triangular BN monolayer grown via an LPCVD technique.⁹⁹ (e and f) SEM images showing the temperature dependent growth of BN at 60 °C and 70 °C, respectively.⁹⁹ (g) Macroscopic BN domains on Ru(0001), coalescence to form a BN film during CVD growth from borazine.¹⁰¹

shown in Fig. 10(a). It was suggested that the hole formation was driven by the lattice mismatch of the BN film and the Rh substrate. BN nanomeshes were later grown on Ru(0001) substrates by the same process and showed similarity to those grown on Rh in many aspects, *e.g.* comprising 2 nm wide apertures with a depth of approximately 0.1 nm, as depicted in Fig. 10(b) and (c).⁸⁶ Further investigation into the BN nanomesh on Rh(111) surfaces demonstrated that it was a single but corrugated monolayer of BN. The 2 nm pores were formed by regions where the layer binds strongly to the underlying metal, while the regular hexagonal network of mesh wires represented regions where the layer was not bonded to the Rh surface but held only through strong cohesive forces within the film itself.¹⁰²

Theoretical and experimental investigations on the h-BN/Rh(111) interface confirmed the formation of a highly corrugated monolayer of h-BN in a 13×12 commensurate geometry (a 13×13 supercell of h-BN on top of a 12×12 supercell of Rh(111)).^{103,104} Such a structure is a result of a delicate balance between repulsive forces acting on N and attractive forces acting on the B atoms. Since the actual absolute values of these forces vary with the lateral BN position, with respect to the Rh substrate surface in the supercell, the h-BN monolayer deforms vertically. As for h-BN/Ru(0001) however, it was demonstrated that h-BN formed a commensurate 14×13 superstructure on Ru(0001) because of the stronger bonding of h-BN to Ru. Compared to h-BN/Rh(111), h-BN/Ru(0001) can accommodate more induced lateral in-plane

strain over larger regions within the superstructure, which itself can consequently become larger.¹⁰⁵

In fact, except for the 1×1 commensurate Ni(111) and Cu(111) systems, the h-BN monolayer shows a regular vertical deformation on other substrates whose structure depends on the symmetry of the substrate. For all hexagonal surfaces a hexagonal superstructure is observed whose size depends on the lattice mismatch between h-BN and the metal surface, whereas some kinds of 1D superstructures are formed for the Pd(110), Mo and Fe(110) surfaces.⁸⁴ For example, Fig. 10(d) and (e) show the special nanopatterned structures of an h-BN monolayer forming long periodic nanowaves on a Fe(110) surface.⁹⁵ The h-BN monolayer on Fe(110) is periodically corrugated in straight washboard (Fig. 10(d)) and kinked washboard (Fig. 10(e)) patterns with long-range order, a periodicity of 2.6 nm, and corrugation amplitude of 0.8 Å. The straight wavy pattern results from strong chemical bonding between h-BN and Fe in combination with a lattice mismatch in either the $[1\bar{1}1]$ or the $[\bar{1}11]$ direction of the Fe(110) surface. The kinked stripes however can be associated with specific Moiré patterns, where the h-BN film is neither matched along $[1\bar{1}1]$ or $[\bar{1}11]$, as illustrated in Fig. 10(f).⁹⁵

High-temperature exposure of a Mo(110) surface to NH_3BH_3 leads to the formation of two distinctly different self-assembling nanostructures.⁹⁶ Depending on the substrate temperature during preparation, either well-aligned, ultra-thin B nanowires form or a single-layer stripe structure of h-BN forms, both of

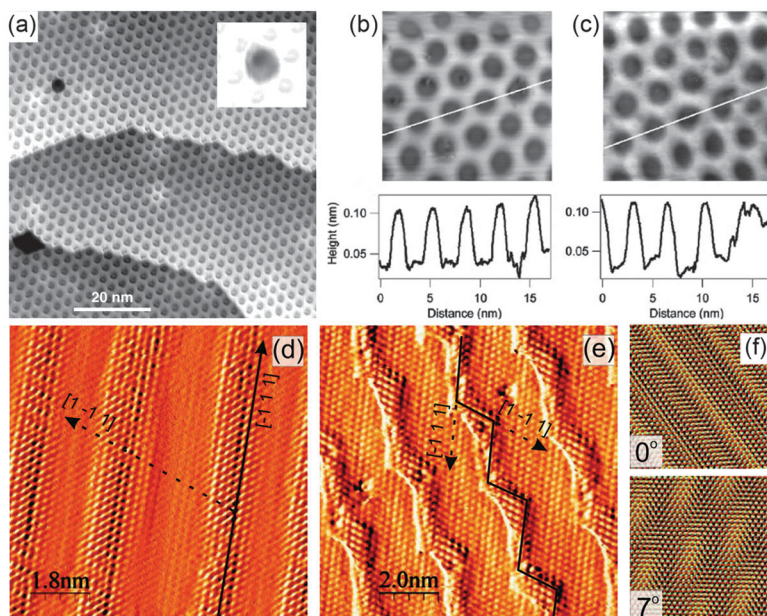


Fig. 10 (a) A constant-current STM image of the BN nanomesh formed on a Rh(111) surface.²⁵ (b and c) Higher magnification STM images of the BN nanomeshes on Rh(111) and Ru(0001), respectively. Their cross-sectional profiles along the white lines show the similarity of the two as they reveal the same apparent buckling of 0.07 ± 0.02 nm between the apertures and the wires, and the same aperture size (2 nm) and wire thickness (1 nm).⁸⁶ (d and e) High-resolution STM images of BN nanowaves formed on Fe(110).⁹⁵ (f) Moiré superstructure models resulting from a superposition of h-BN(0001) and Fe(110) lattices as a function of rotational (polar) angle between them. B, N, and Fe atoms are coloured red, blue, and yellow, respectively.⁹⁵

which show 1D characteristics, but in directions perpendicular to one another. The h-BN phase forms stripes along the [1̄1̄0] direction and the B nanowires are aligned along the perpendicular [001] direction. In a similar way, h-BN monolayers have been formed on Cr(110) surfaces.⁹⁷ However, in this case, instead of B nanowires, a 1D structure of h-BN was formed. The h-BN layer exhibited long range order along [001] and short range order in the [1̄1̄0] direction, *i.e.* the 1D h-BN structure on Cr(110) was aligned as the B nanowires phase on Mo(110), and it was perpendicular to the h-BN phase on Mo(110).

3.3.3 Epitaxial growth of BN multilayers. Large area synthesis of few-layered BN films (2–5 layers) on a copper (Cu) foil *via* a thermal catalytic CVD method and successful transfer to different substrates was first reported in 2010.¹⁰⁶ The Cu substrate was placed in the centre of a split tube furnace, and annealed at 600 °C for 20 min under an Ar–H₂ flow, followed by a gradual heating up to 1000 °C. Ammonia borane (NH₃–BH₃) was sublimated at 120–130 °C using a heating belt, then carried into the reaction region by the Ar–H₂ flow and held for 30–60 min to form the few-layered BN. The similarity of the lattice constants of BN and Cu ($\sim 2\%$ mismatch) is essential for growing large flat nanosheets. The obtained few-layered BN sheets are shown in Fig. 11(a) and (b).

Other metallic substrates have also been utilized for the growth of BN nanosheets. Few-layered BN was grown on polycrystalline Ni films by using B₃N₃H₆ vapour in an ambient pressure CVD setup.¹⁰⁷ Depending on the growth conditions, the thickness of the obtained BN films was between 5 and 50 nm. The BN film can grow continuously on the entire Ni surface with regions of uniform thickness as large as 20 μm in lateral size (*i.e.*, the size

of the Ni crystal grains). AFM images of the BN nanosheets grown on Ni substrates *via* the reaction of polyborane decaborane (B₁₀H₁₄) and NH₃ are shown in Fig. 11(c) and (d). These few-layered BN nanosheets exhibit well-defined angular edges, with near regular angles of 30, 60, or 90°.¹⁰⁸ Similar regular features have been observed during the growth of BN domains on Ni(111) in UHV systems.^{73,109} Recently, confocal Raman spectroscopy was used to probe the effect of underlying Ni crystals with various orientations on the CVD growth of BN layers from NH₃BH₃.¹¹⁰ The results demonstrated that BN growth strongly depends on the Ni crystal orientation. In fact, BN growth rate was larger on Ni(100)-like crystal surfaces, while the growth on Ni(111)-like surfaces was not detectable. This suggests that Ni(100)-like facets are likely to promote BN growth, possibly due to their high surface energy. Thus, NH₃BH₃ may quickly adhere to the Ni(100) surface to reduce its energy, which leads to the fast nucleation and growth of BN sheets. Such observations for the LPCVD BN growth on Ni substrates are in clear contrast to the UHV growth of BN on Ni(111), which suggestss the importance of the growth conditions on the BN layer formation. In another approach, monolayer, bilayer and few-layered h-BN domains and large-area continuous films could be selectively grown on polycrystalline Pt foils using a low-cost ambient pressure CVD method with B₃N₃H₆ as the precursor.¹¹¹

3.3.4 Non-epitaxial growth. Several systems have been developed for the non-epitaxial CVD growth of 2D BN nanomaterials. In most cases, the BN layers are grown on a substrate; however, there are a few substrate-free methods too. The first successful synthesis of BN nanoflakes *via* a catalyst-free

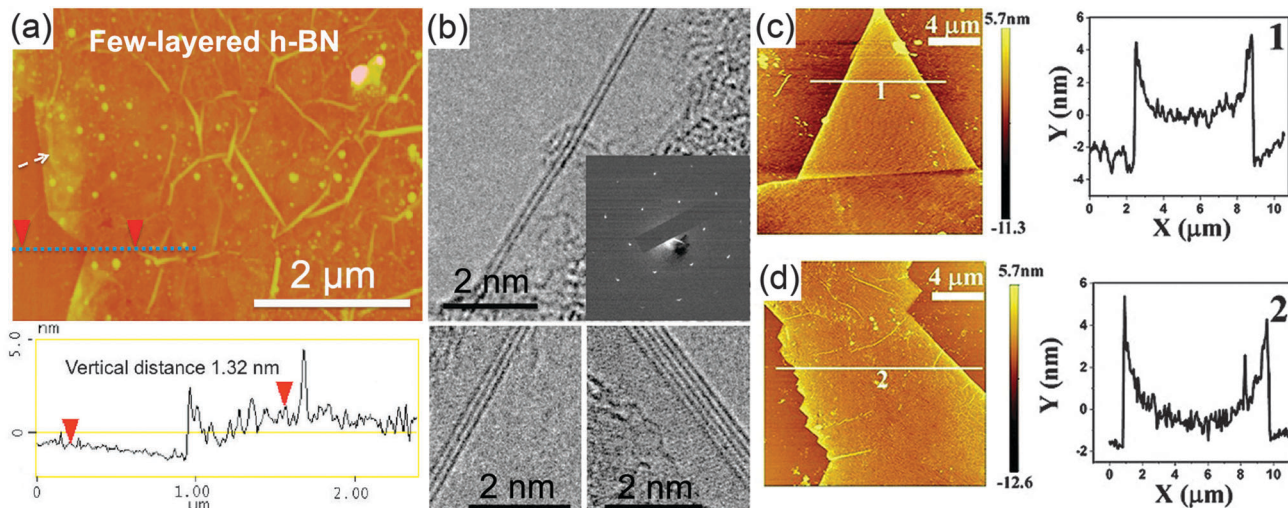


Fig. 11 (a) AFM image and line-scan profile of a few-layered BN film with a uniform thickness of 1 nm.¹⁰⁶ (b) HRTEM images of the film edges, indicating 2–5 atomic layer thickness.¹⁰⁶ (c and d) AFM images and height profiles of BN nanosheets grown on Ni foil, exhibiting an average thickness of 2 nm and angular edges: (c) triangular BN nanosheet; (d) zigzag and straight edges.¹⁰⁸

CVD process at 1100–1300 °C was performed in 2009.¹¹² B_2O_3 and melamine powders were used as precursors at the centre of an induction furnace. Argon (Ar) was introduced as a carrier gas, and N_2 as the reaction gas. The thickness of the BN sheets could be controlled in the range of 25–50 nm by the synthesis temperature. The morphology of the BN nanoflakes is shown in Fig. 12(a). In another approach, the reaction of H_3BO_3 and urea ($\text{CH}_4\text{N}_2\text{O}$) at 900 °C under N_2 atmosphere resulted in few-layered BN nanosheets.¹¹³ It was claimed that the number of layers could be controlled by varying the concentration of the reacting materials. Namely, the thickness of the sheets decreased as the urea concentration in the reaction mixture was increased.

Vertically-aligned BN nanosheets on a silicon (Si) substrate were grown at 800 °C from a gaseous mixture of $\text{BF}_3\text{-N}_2\text{-H}_2$ via a microwave plasma CVD (MPCVD) technique.¹¹⁴ The growth of such protruding BN nanosheets rather than a uniform granular film was attributed to the strong etching effect of fluorine and the electrical field generated in the plasma sheath. Altering the ratio and flow rates of BF_3 and H_2 affected the morphology and thickness of the BN nanosheets. By increasing the BF_3 flow rate, branching of nanosheets was observed, *i.e.*, subnanosheets grew on the surface of the main nanosheets, as shown in Fig. 12(b). Moreover, the thickness of the nanosheets decreased from 20 to 5 nm by decreasing the flow rate ratio of BF_3/H_2 from 5 : 10 to 2 : 30 sccm. Alternatively, a thermal CVD technique was developed in which solid precursors (B, MgO and FeO powders) were heated up to 1000–1300 °C in a horizontal tube furnace under an NH_3 flow.^{36,115} As a result vertically-standing BN nanosheets were grown on Si/SiO_2 substrates with different sizes and morphologies, depending on the synthesis temperature. As the temperature increased from 1000 to 1200 °C the nanosheets grew larger in lateral size, and at 1300 °C branching of subnanosheets on the surface of the main nanosheets resulted in a peculiar 3D nanostructure (Fig. 12(c) and (d)). The thicknesses of the nanosheets were mostly less than 4 nm,

and the nanosheets grown at higher temperatures displayed better crystallinity. In another set of experiments, B and B_2O_3 powders were used as precursors at 1200 °C under an NH_3 flow to produce BN nanosheets with thicknesses smaller than 5 nm protruding from the Si/SiO_2 substrate. This suggests that the BN nanosheet growth is not strongly dependent on specific precursor materials, as long as enough reactive B and N are provided in the growth atmosphere. Fig. 12(e) illustrates the proposed model for the two-stage growth of such BN nanosheets.¹¹⁶ That is, before the onset of the vertical growth of the nanosheets, there is a planar growth stage, in which the base layers are flat and parallel to the substrate. After the development of sufficient levels of force at grain boundaries, the edges of the top layers curl upward and the vertical growth of the nanosheets begins. BN species at the synthesis temperature (≥ 1000 °C) can be assumed to have very high mobility; therefore, upon landing on the surface of a growing nanosheet, they quickly move along the surface towards the edge of the nanosheet and covalently bond to the edge atoms before being re-evaporated. Thus, the BN nanosheets tended to grow taller rather than thicker.^{115,116}

Hollow nanoribbons of BN have been fabricated by a combined CVD-templating method using ZnS powder and a B-N-O-Fe mixture (produced by ball milling of B, B_2O_3 and Fe_2O_3 in an NH_3 atmosphere). The precursor materials were mixed and placed inside a furnace with Ar, NH_3 and H_2 flow as the carrier and reaction gases, respectively. The furnace temperature was raised to 1220 °C for 2 hours to form ZnS -BN core-shell heterostructures. Subsequently, the temperature was increased to 1350 °C and maintained for 4 hours in a vacuum at 50 Torr to remove the ZnS template.²⁷ The synthesized BN product is displayed in Fig. 13.

3.4 Solid-state reactions

Flower-like BN nanoflakes were produced by a template-free solid phase reaction. NaBF_4 , NH_4Cl and NaN_3 powders were

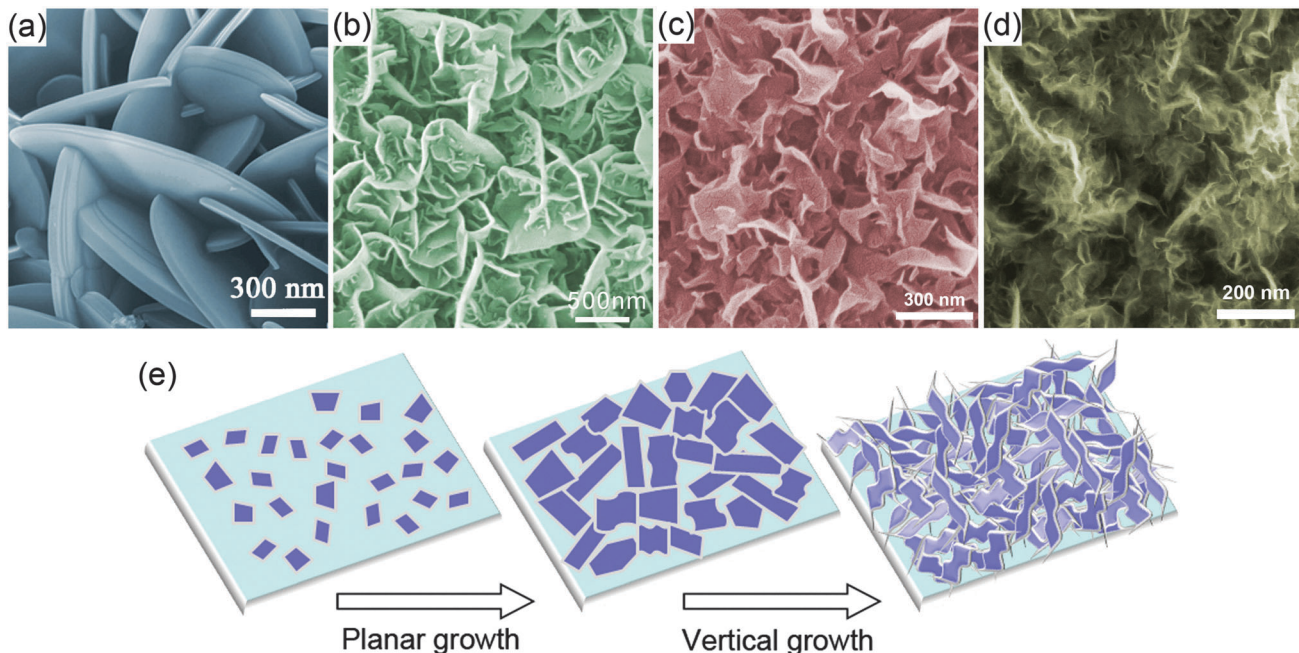


Fig. 12 SEM images of non-epitaxially grown (a) BN nanoflakes;¹¹² (b) vertically-aligned BN nanosheets on a Si substrate, grown at 800 °C;¹¹⁴ (c and d) partially vertically-aligned BN nanosheets on a Si/SiO₂ substrate, grown at 1200¹¹⁵ and 1300 °C.³⁶ (e) A model illustrating the nucleation and two-stage growth of the BN nanosheets on the Si/SiO₂ substrate.¹¹⁶

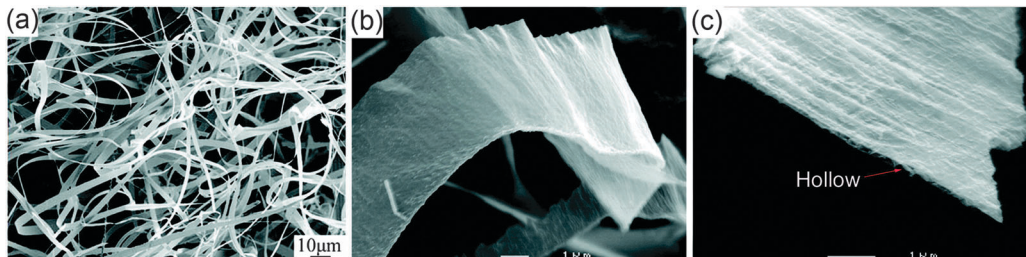
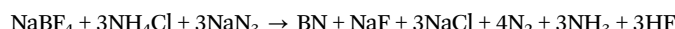


Fig. 13 Low-magnification (a) and high-magnification (b and c) SEM images of the hollow BN ribbons produced using a CVD-templating method.²⁷

mixed, pressed into pellets at room temperature, and then heated in an autoclave at 300 °C for 20 hours. The BN production reaction is:



The as-prepared BN nanoflowers were composed of vertically standing BN nanoflakes. In order to prepare few-layered BN nanosheets, the nanoflakes were sonicated in water for 2 hours, followed by ultrasonic treatment in DMF, dimethyl sulfoxide (DMSO) and 1,2-dichloroethane (EDC) for 3 hours, and finally centrifugation at 4000 rpm for 15 minutes to remove any residual large-size BN particles.¹¹⁷ This method was later modified by introducing sublimed sulfur (S) into the reaction mixture as the initiator, which resulted in a decrease in the thickness of the BN nanosheets.¹¹⁸

Fig. 14 displays a chemical blowing method by which few-layered BN nanosheets with large lateral dimensions (over 100 μm) were produced. This technique does not require a catalyst or substrate, instead it uses moderate heating of

NH₃BH₃ at atmospheric pressure. The precursor is preheated at 80 °C, then the temperature is increased to ~110 °C to begin the blowing process due to dehydrogenation, and finally to ~400 °C to dehydrogenate, where hydrogen is rapidly released from the soft swollen B–N–H compound. Further heating to 1400 °C for 3 hours crystallizes the material into a desired BN product. Ultrasonic stirring in ethanol for 1 minute and centrifugation at 1000 rpm for 1 minute removed the bulky portions from the BN suspension, and yielded few-layered polycrystalline BN nanosheets.^{37,119}

In another approach, BN nanoplates with thicknesses of ~30 nm and lateral sizes of a few hundred nm have been synthesized *via* combustion and annealing processes with a viscous gel composed of H₃BO₃, CH₄N₂O, sodium azide (NaN₃) and ammonium chloride (NH₄Cl) in water. The solution was ignited at 600 °C in an electric muffle furnace and the resultant product was washed with de-water and ethyl alcohol, dried in a vacuum, and annealed between 1000 °C and 1400 °C in an N₂ atmosphere to obtain the BN nanoplates.¹²⁰

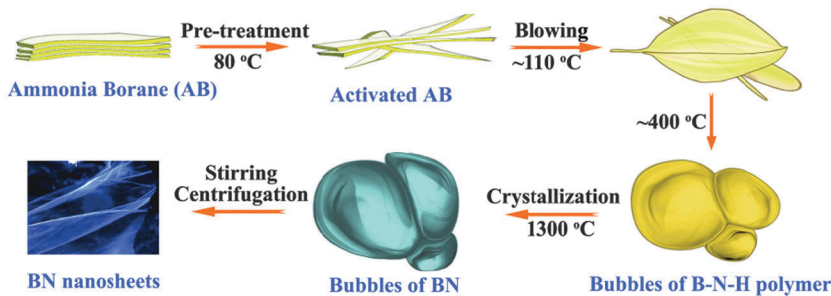


Fig. 14 Synthesis scheme of BN nanosheets via a chemical blowing method.³⁷

Alternatively, thin BN nanosheets with an average thickness of 4 nm were prepared using B_2O_3 , Zn and $\text{N}_2\text{H}_4 \cdot 2\text{HCl}$ in a stainless steel autoclave at 500 °C for 12 hours followed by HCl treatment, filtration and drying at 80 °C.¹²¹

3.5 Substitution reactions

In a substitution reaction, an atom or a functional group in a particular chemical compound is replaced by another atom or group. In a series of experiments, B_2O_3 powder was placed in an open graphite crucible, covered with molybdenum oxide (MoO_3) as a promoter and then with graphene sheets. The crucible was held in a flowing N_2 atmosphere at 1650 °C for 30 minutes. Afterwards, the product was collected from the bed of graphene sheets and heated in air at 650 °C for 30 minutes to remove the remaining C layers, and obtain pure BN.¹²²

3.6 High-energy electron irradiation

Freestanding BN monolayers can be fabricated by controlled energetic electron irradiation using a layer-by-layer sputtering process inside a TEM. Initially, BN nano-flakes and powders undergo mechanical cleavage to obtain BN sheets with a reduced number of layers. Then they are further thinned down to monolayers by intensive electron beam irradiation. In this process, the incident electron beam with a few-nm diameter is focused onto the specimen, and the beam intensity is set to a high value. By manual scanning of the electron beam on the specimen, the BN nano-flakes (which are few nanometers thick) are burnt layer-by-layer, starting from the topmost layer, until BN monolayers are obtained.^{52,53}

3.7 Unzipping BN nanotubes

Inspired by the unzipping of multiwalled C nanotubes to produce narrow graphene nanoribbons,¹²³ BN nanotubes were also unwrapped *via* Ar plasma etching.¹²⁴ In this process, multiwalled BN nanotubes were first deposited on a Si substrate and spin-coated with a poly(methyl methacrylate) (PMMA) film. The polymer film with embedded nanotubes was peeled off and turned over. Then, the composite PMMA-BN nanotube film was subjected to Ar plasma etching for 100 seconds. While the bottom surface of the BN nanotube was covered and protected by the polymer matrix, the ablation of the top surface of the nanotubes led to the formation of half-opened BN nanoribbons. PMMA was removed by acetone

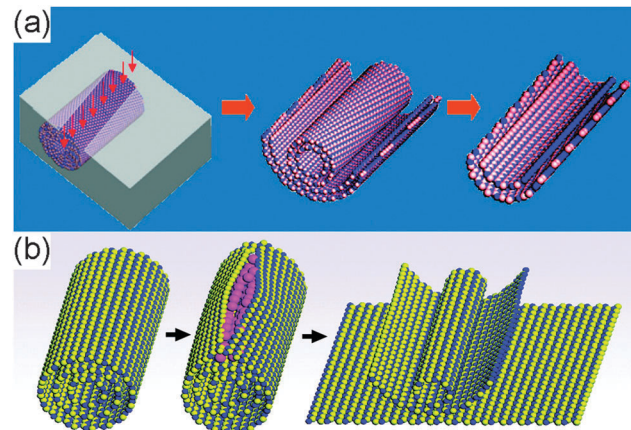


Fig. 15 (a) Schematic of the BN nanotube unzipping processes induced by plasma etching. The stepwise opening/unzipping, removal and exfoliation of tube walls forming nanoribbons are sketched.¹²⁴ (b) Schematic of the splitting process of a BN nanotube to form nanoribbons. The pristine BN nanotube begins to locally unzip due to K intercalation induced pressure buildup, which results in further splitting of the nanotube in the longitudinal direction to form few-layered nanoribbons.¹²⁵

vapour, and the BN nanoribbons produced were heated at 600 °C for 6 hours to remove the PMMA residue and oxidize possible carbonaceous contaminants. The nanoribbons were as narrow as 15 nm with lengths up to a few μm . Fig. 15(a) illustrates the unzipping process.

Alternatively, BN nanoribbons were produced by the longitudinal splitting of BN nanotubes through intercalation of potassium (K) vapour into their walls.¹²⁵ In this process, BN nanotubes were placed into an ampoule with excess freshly cut K pieces, evacuated to 10^{-6} Torr, and heated at 300 °C for 72 hours. Then, the material was heated at 600 °C for 30 min to remove carbonaceous impurities. Few-layered BN nanoribbons were obtained with lengths over 1 μm , widths between 20 and 50 nm, and thicknesses of between 2 and 10 layers. The equilibrium interplanar spacing for K-intercalated BN has been calculated to be 5.8 Å.¹²⁶ For a BN nanotube, this significant increase in wall spacing from ~ 3.33 Å would result in significant circumferential strain on the atomic bonds. It was suggested that similarly to the case of K-intercalated C nanotubes, islands of intercalated K could grow from an initial starting point of K intercalation. This increases the circumferential strain until the

bonds break at the weakest points (such as sp^3 bonding sites). Then, K atoms can bond to the bare ribbon edges and the hindrance arising from these moieties induces further splitting longitudinally.¹²⁷ Fig. 15(b) illustrates a schematic of the splitting process.

4. Properties and applications

Bulk h-BN has been a matter of interest for a long time due to its low density, high thermal conductivity, electrical insulation, superb oxidation resistance, excellent inertness, and low friction coefficient. 2D BN nanostructures, as inheritors of h-BN, also possess a unique combination of those advantageous properties, which promotes their usage in various applications.⁵⁸ The most promising application is their use as dielectric substrates in graphene electronic devices. Furthermore, BN nanosheets can be utilized as multifunctional composite fillers, thermally robust catalytic and sensing substrates, highly durable field emitters, chemically inert superhydrophobic films, etc.⁴² In this section an overview of such properties and applications is presented.

4.1 Electronic properties and applications

BN nanostructures are generally recognized as wide bandgap (5.0–6.0 eV) semiconductors. Theoretical analysis of the electronic properties of BN nanotubes and nanosheets suggests that their bandgap is first-order independent of the details of the atomic structure.¹²⁸ Recently, BN was employed as an improved dielectric for graphene devices.¹²⁹ Since BN is chemically and thermally stable, and free of dangling bonds and surface charge traps, graphene devices on BN show roughness and fluctuations which are potentially two orders of magnitude lower than comparable devices on SiO_2 , which in turn leads to improved mobility, field-effect transistor performance, and chemical stability.^{129–133} Atomically thin multilayered BN nanosheet-graphene heterostructures with sandwich configurations (e.g. BN–C–BN) have exhibited extraordinary charge mobility, as high as $\sim 500\,000\,cm^2\,V^{-1}\,s^{-1}$.¹³² Another heterolayered configuration (C–BN–C) has been utilized in field-effect tunnelling transistor devices,¹³⁴ in which two graphene layers are separated by a thin BN nanosheet. Measurements of the electron tunnel current through BN nanosheets demonstrate that they are good tunnel barriers down to a single atomic plane. However, the tunnel current is exponentially dependent on the BN barrier thickness, as expected for quantum tunnelling.¹³⁵ Moreover, a BN nanosheet can serve as a tunnel barrier between graphene and a metal gate in a graphene tunnel junction.¹³⁶

In comparison to insulating BN nanosheets, BN nanoribbons with either zigzag or armchair edges exhibit a much more considerable quantum confinement from the edge effect, which influences their anisotropic electronic properties. Theoretical studies suggest that the energy bandgap of zigzag BN nanoribbons is indirect and decreases monotonically with increasing ribbon width, whereas armchair BN nanoribbons have a direct energy bandgap.¹³⁷ First-principles calculations show that although BN nanoribbons are insulators regardless of their width and edge shape, an insulator–metal transition in the ribbon can be

gradually realized by increasing the transverse electric field.^{138,139} That is, upon the application of a weak field, the field-induced redistribution of edge states in zigzag BN nanoribbons reduces the energy gap, while a Stark effect induces the gap narrowing of armchair BN nanoribbons. Then, as the field gets stronger, the energy gaps of both nanoribbon types gradually close due to the field-induced motion of nearly free electron states.¹³⁸ The formation of Stone–Wales defects can also significantly narrow the energy gaps of the defective BN nanoribbons, although they still retain a typical wide-bandgap semiconductor behavior.⁴¹ In addition, hydrogen modification of BN nanoribbons can induce changes in electronic properties and bandgap reduction.¹⁴⁰ These changes are more significant in zigzag nanoribbons, as they display half-metallicity with hydrogen termination, while armchair nanoribbons are usually much more robust and maintain their semiconductivity.^{141–143} However, it has been calculated that armchair nanoribbons can also become half-metallic through termination with some transition metals, such as Fe.¹⁴⁴

Another approach to modify the wide bandgap of 2D BN nanomaterials is the addition of a third element into their structure. Bearing in mind the similar lattice parameters and crystal structure of BN and graphene, it can be expected that C addition into the BN network would form stable structures. In fact, the combination of the semi-metallic properties of graphene with the electrical insulation of BN has drawn particular attention to the ternary B–C–N system.¹⁴⁵ Boron carbonitride ($B_xC_yN_z$) nanostructures are especially attractive for applications in electronic and luminescent devices owing to their semiconducting properties with variable band gap energies.¹⁴⁶ The experimental results from the bandgap measurement of pure BN nanoribbons and nanosheets have shown wide gaps of $\sim 5.3\,eV^{27}$ and $\sim 5.7\,eV^{145,146}$ respectively; while, the incorporation of C into the BN matrix can result in BN–C hybridized nanosheets with much smaller band gaps.^{119,145–147} A common feature in the aforementioned hybrid nanomaterials is the phase separation of C in the BN matrix, which leads to the formation of graphene islands in BN layers. As a result, a dual bandgap characteristic has been observed: a small bandgap related to the C domains distributed in the BN lattice and a larger one related to the BN matrix containing the C islands. Depending on the C content and the sheet thickness, the reported bandgaps are different. For example, the measured bandgaps in hybridized multilayered BN nanosheets with 14 at% C were 1.19 eV and 4.25 eV,¹⁴⁵ while double- and triple-layered nanosheets with 84 at% C exhibited 3.85 eV and 1.51 eV bandgaps.¹⁴⁶

4.2 Optical properties and applications

2D BN nanostructures, like bulk h-BN, do not exhibit any optical absorption in the visible region of the electromagnetic spectrum (390–700 nm). Therefore, they exhibit high transparency as thin films or suspensions, and appear white when accumulated in bulk quantities.^{57,62,99,106,107,148} That is why BN nanosheets are sometimes referred to as “white graphenes” in the literature. In the deep UV range however, BN nanosheets show a sharp absorption peak at ~ 210 –220 nm.^{99,106,107,145}

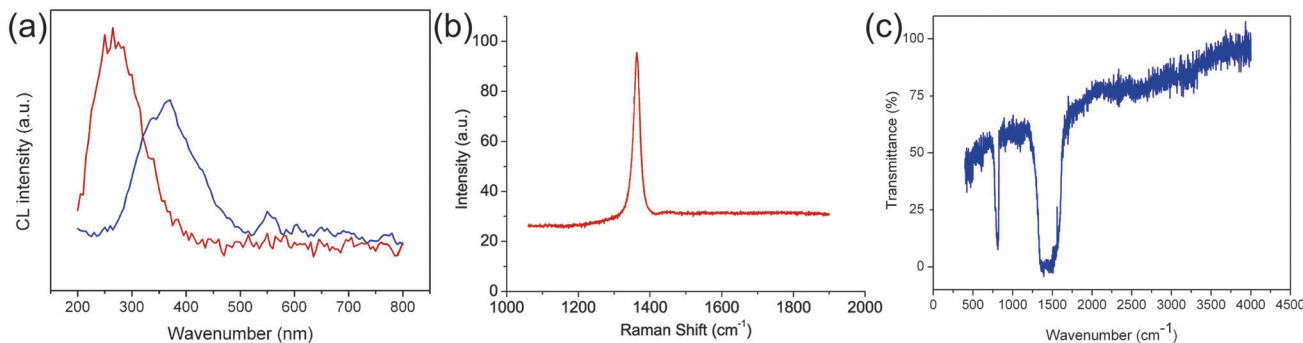


Fig. 16 (a) CL spectra of vertically-standing BN nanosheets (red) and a granular BN film (blue).¹¹⁴ (b) Raman spectrum of multilayered BN nanosheets.¹¹⁵ (c) FTIR spectrum of vertically-standing BN nanosheets.¹¹⁴

Pure h-BN single crystals exhibit a dominant luminescence peak and a series of s-like exciton absorption bands at ~ 215 nm.¹⁴⁹ In a similar fashion, BN nanosheets show a strong cathodoluminescence (CL) emission in the deep ultraviolet range.^{112,114,145} This makes these 2D nanomaterials appealing for compact UV laser devices, which are essential in applications such as optical storage, photocatalysis, sterilization, ophthalmic surgery and nanosurgery.¹⁴⁹

Fig. 16(a) shows a comparison between the CL spectra of a vertically-standing BN nanosheet coating and a granular BN film.¹¹⁴ The BN nanosheets exhibit an emission band in the range 200–400 nm whereas the granular BN film shows a broadened CL emission band in the range 260–520 nm. The emission peak at ~ 215 nm is from free excitons,¹⁴⁹ those at 220 and 227 nm are from bound excitons,^{149,150} and the 300–400 nm peaks appear because of vacancies or residual impurities such as oxygen and carbon in the BN structure.^{27,145,149,151}

Other spectroscopic signatures of BN nanosheets, such as Raman and Fourier transform infrared (FTIR) characteristic peaks, are also quite similar to those of bulk h-BN crystals. Fig. 16(b) shows a typical Raman spectrum of CVD-grown multilayered BN nanosheets with a 1365 cm^{-1} characteristic peak, which is very similar to the 1366 cm^{-1} Raman shift of h-BN single crystals.¹¹⁵ Crystalline h-BN has D_{6h}^4 space group symmetry and the symmetry transformations of the zone-center optical phonons are given by eqn (1):

$$\Gamma = 2E_{2g} + 2B_{1g} + A_{2u} + E_{1u} \quad (1)$$

Among which, the E_{2g} modes are Raman-active, the A_{2u} and E_{1u} modes are IR-active, and the B_{1g} modes are optically inactive. Both of the Raman-active E_{2g} modes are due to in-plane atomic displacements; the low frequency mode is characterized by whole planes sliding against each other, and the high frequency mode is due to B and N atoms moving against each other within a plane. The low frequency mode is in the range $49\text{--}52.5\text{ cm}^{-1}$, although it has been less observed because of its low intensity and high Rayleigh background, whereas the high frequency intralayer E_{2g} vibration mode of different h-BN structures is in the range $1363\text{--}1374\text{ cm}^{-1}$.^{114,115} The red shift in the multilayered BN nanosheets (compared to bulk BN crystals) may be due to (1) the interactions of the

neighbouring layers in few-layered nanosheets which lead to a small elongation of the B–N bonds and consequently a softening of the phonons, (2) the local temperature increase caused by the laser, and (3) generation of stress in nanosheets due to their intrinsic wrinkles or interactions with the substrate.¹¹⁵ However, BN monolayers have shown sample-dependent blue shifts of up to 4 cm^{-1} (*i.e.*, the Raman shift at 1370 cm^{-1}) attributed to a hardening of the E_{2g} phonon mode due to a slightly shorter B–N bond expected in the isolated monolayers.⁵⁷ It is also known that a Raman peak frequency would shift to higher and lower frequencies under compressive and tensile stresses.¹⁵²

Fig. 16(c) is a typical FTIR spectrum of BN nanosheets. A sharp absorption peak is observed at 811 cm^{-1} and a broad absorption band with the bottom in the range $1350\text{--}1520\text{ cm}^{-1}$, which are ascribed to the A_{2u} (B–N–B bending vibration mode parallel to the *c*-axis) and E_{1u} (B–N stretching vibration mode perpendicular to the *c*-axis) modes of h-BN, respectively.¹¹⁴ The FTIR spectrum of hollow BN nanoribbons shows A_{2u} and E_{1u} modes at 818 and 1367 cm^{-1} , respectively.²⁷ These results are similar to the characteristic peaks of polycrystalline h-BN at 811 and 1377 cm^{-1} .¹⁵³

4.3 Thermal properties and applications

Excellent thermal transport properties in graphene arouse widespread interest in thermal transport of other honeycomb lattice structure materials such as BN. The room temperature thermal conductivity (κ) of bulk h-BN can reach $\sim 400\text{ W m}^{-1}\text{ K}^{-1}$. This value is much larger than that of most metallic and ceramic materials, but it is still five times smaller than that of pyrolytic graphite. This is surprising given the similar crystal structures, lattice constants, unit cell masses, and phonon dispersions shared by these materials.^{154,155} In the absence of experimental data from direct measurements of κ values of BN monolayers, theoretical studies suggest that BN monolayers have a significantly larger κ value than their bulk counterparts because of a reduction in phonon–phonon scattering in the 2D layer. This feature gives BN monolayers one of the highest room temperature thermal conductivities, other than those in the carbon allotropes.¹⁵⁴

Theoretical works on the comparison between BN- and C-based nanomaterials also show that the BN-based nanostructures

have a lower thermal conductivity than their C analogues. Two possible reasons for this disparity are the softer phonon modes, especially in the acoustic branches of BN-based systems, and the mass difference of B and N.¹⁵⁵ Studies on BN sheets suggest a large contribution from out-of-plane vibrations in the calculation of the κ value, which are smaller in multilayered BN sheets than in monolayered ones due to interlayer coupling. Moreover, the calculated κ for multilayered BN decreases monotonically from monolayered BN with the increasing the number of layers and converges to the calculated κ for h-BN within a few layers.¹⁵⁶ A comparison between BN and graphene nanoribbons shows that as the temperature falls below 300 K the thermal conductance of the BN nanoribbons becomes larger than that of graphene nanoribbons, while at higher temperatures the former is lower than the latter. In addition, for both armchair- and zigzag-type BN nanoribbons, thermal conductance depends linearly on their width and is calculated to be about 20% larger in zigzag-type nanoribbons than in armchair nanoribbons at 300 K, indicating anisotropy in the thermal transport in BN nanoribbons.¹⁵⁷

An important application of BN nanomaterials is as fillers in thermally conductive polymers.^{29,158–161} Since standard polymer materials normally have low thermal conductivity, traditional fillers such as Si₃N₄, AlN, and BN microparticles have been embedded in them to improve their thermal conductivity. However, compared to microparticles, nanomaterials are more effective fillers for such polymer matrix composites due to their higher surface area.¹⁶¹ The polymers embedded with graphenes or other conductive fillers may exhibit high thermal conductivities and dielectric constants before the percolation threshold;¹⁶²

however, the possible electrical current leakage is undesired. BN nanosheets on the other hand, exhibit good electrical insulation to compensate for such drawbacks.

Because of the high thermal conductivity of the BN sheets they have been recently used as 2D fillers in a mineral oil to form a stable Newtonian nanofluid for application in transformers. This nanofluid is also electrically insulating and has a lower freezing point than that of the pure mineral oil. These unique nanofluids may be the next generation of thermal nano-oils for lubrication, capable of efficient thermal management in heavy duty machinery such as transformers, since these oils require excellent filler dispersion, high thermal conduction, and electrical insulation.¹⁶³ Photographs of the pure mineral oil and its suspensions with BN nanosheets are shown in Fig. 17(a). Fig. 17(b) shows that the thermal conductivity of the mineral oil is not temperature-dependent whereas the thermal conductivity of the nanofluids largely depends on the temperature, which indicates the role of the BN nanosheets in thermal conductivity. Fig. 17(c) depicts the thermal conductivity enhancement with increasing BN nanosheet concentration in the mineral oil.

4.4 Mechanical properties and applications

Theoretical analyses and experimental results have shown that graphene is the stiffest material with calculated and measured Young's moduli of 1.05–1.24^{164–166} and 1 TPa,¹⁶⁷ respectively. These results suggest that other defect-free 2D nanomaterials with honeycomb structures, such as BN nanosheets, also have potential to be extraordinarily resilient and strong.^{168–171} To investigate the mechanical properties of BN nanosheets,

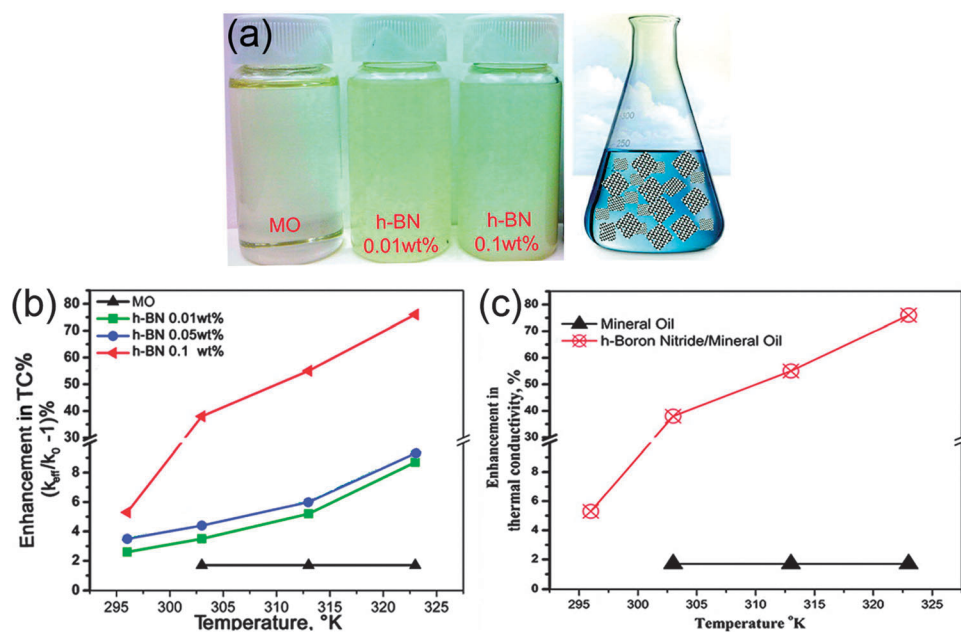


Fig. 17 (a) Photographs of pure mineral oil and suspensions of 0.01 and 0.1 wt% BN nanosheets in the mineral oil, and a schematic of 2D nanosheets in mineral oil. (b) Temperature-dependent effective thermal conductivity (TC) enhancement of various nanofluids (percentage filler amount is mentioned). (c) Enhancement in thermal conductivity with increase in the BN concentration in mineral oil measured at 323 K. This indicates the formation of percolation channels for thermal conduction by high surface area h-BN flakes.¹⁶³

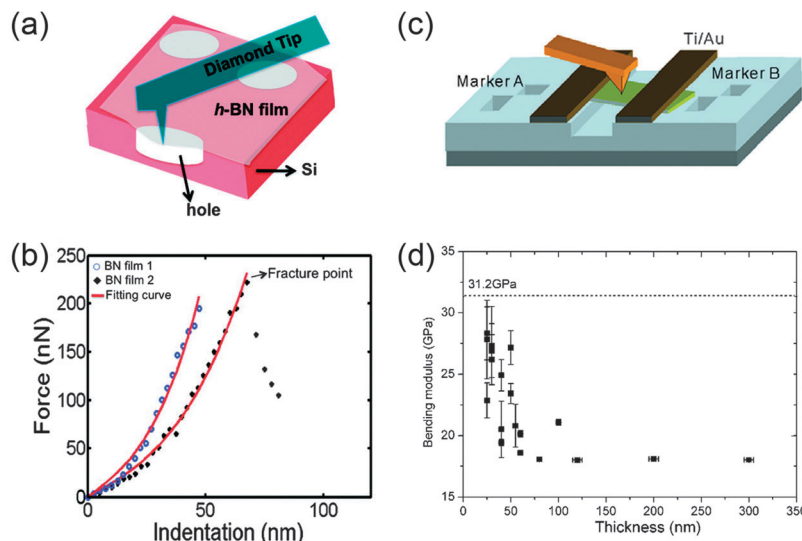


Fig. 18 (a) Schematic of nanoindentation on a suspended BN nanosheet.¹⁰⁶ (b) Measured force vs. displacement and fracture loading curves for two BN nanosheet samples.¹⁰⁶ (c) Schematic of the AFM bending test of a clamped BN nanosheet.¹⁷² (d) Bending modulus vs. BN nanosheets thickness. The theoretical C_{33} value reported for bulk h-BN is also shown for comparison (dashed line).¹⁷²

nanoindentation measurements using atomic force microscopy (AFM) have been carried out.¹⁰⁶ As schematically shown in Fig. 18(a), the CVD-grown BN layers were transferred onto a Si substrate containing circular wells of 1 μm diameter, the layers were then indented with a diamond tip. The calculated values of the elastic constant (E^{2D}) for the few-layered BN nanosheets with thicknesses of 1–2 nm are in the range of 220–510 N m⁻¹. Typical indentation test curves in Fig. 18(b) indicate that the BN layers break at deflections of ~ 70 nm and forces of ~ 220 nN. Further simulation of the mechanical behavior of the BN nanosheets under nanoindentation have shown that both the modulus and the breaking strength of the nanosheets decrease with the vacancy concentration in their structure.¹⁰⁶

In another approach, bending moduli of exfoliated BN nanosheets with thicknesses of 25–300 nm and lateral sizes of 1.2–3 μm were measured using three-point bending tests inside an AFM.¹⁷² As schematically displayed in Fig. 18(c), BN nanosheets were suspended on a trenched SiO_2 substrate and were clamped by a metal film. The bending test results in Fig. 18(d) show that the bending modulus of the BN nanosheets increases with the decrease in sheet thickness and approaches the theoretical value of h-BN single crystals in sheets of less than 50 nm thickness.

In situ bending tests of few-layered BN nanoribbons inside a TEM have shown that they bend reversibly by forming a localized kink, caused by the wrinkling of individual BN layers. This demonstrates the extraordinary flexibility of 2D BN nanostructures. Molecular dynamics simulations of this bending test revealed that the bending is smooth and platelike at low curvatures, that is the BN layers bend collectively and do not slide relative to each other, followed by kinking.¹⁷³

Due to the great mechanical performance of BN nanosheets, they have been utilized to reinforce polymer films.^{29,37,63,174}

For instance, the elastic modulus of PMMA films was increased by 22% and their strength by 11% after the incorporation of only 0.3 wt% of BN nanosheets into the polymer.²⁹ Moreover, a recent study shows that BN nanoplates can be used to improve the fracture toughness of ceramic matrix composites. $\text{ZrB}_2\text{-SiC}$ composites reinforced with a mixture of 1D and 2D BN nanomaterials were prepared by spark plasma sintering and exhibited improved fracture toughness by up to $\sim 24.4\%$ at 1 wt% BN.¹⁷⁵

4.5 Wetting properties and applications

Wetting is the ability of a liquid to maintain contact with a solid surface, which results from the intermolecular interactions at their interface. The degree of wetting (wettability) is determined by the interplay between adhesive forces (liquid–solid) and cohesive forces (liquid–liquid). In general, the wettability of a surface depends on its chemical composition and microstructural geometry. Although water can relatively wet bulk BN surfaces, BN nanostructure containing surfaces may repel water droplets.^{114–116,176–178} In fact, a smooth BN coating is relatively hydrophilic with a water contact angle (CA) of $\sim 50^\circ$, whereas nanorough BN coatings made of partially vertically aligned nanosheets can be hydrophobic (CA $> 90^\circ$) or even superhydrophobic (CA $> 150^\circ$). Fig. 19 shows SEM, AFM, and water CA images of a series of BN nanosheet coatings with different levels of surface roughness. As a result of the morphological changes in the coatings, the CA altered from 51° to 159° . This considerable shift in wetting properties has been explained by the Cassie–Baxter model, which considers surface roughness and the real contact area of the solid and liquid at their interface as two factors which promote superhydrophobicity on a non-flat surface.¹¹⁵

In contrast with the experimental results, the simulated CA on a flat BN monolayer is 86° , much larger than the reported

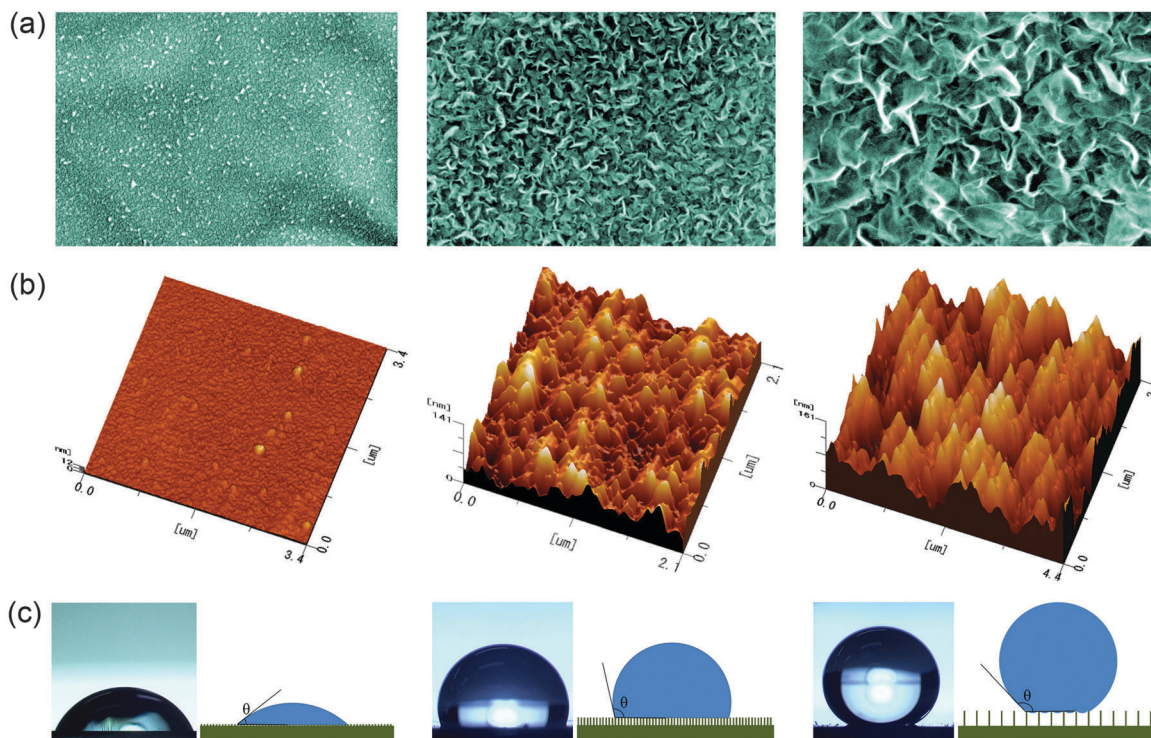


Fig. 19 (a) SEM, (b) AFM and (c) water CA images of a series of BN nanosheet coatings with different levels of surface roughness. From left to right, as the roughness increases and the fraction of solid in contact with the liquid at the interface decreases, an enhancement in the water-repellency of the BN nanosheet coatings is observed.¹¹⁵

experimental values. But, the simulation of a water droplet on a wrinkled BN monolayer results in a notably smaller contact angle. The polar nature of the B–N bonds and the enhancement of their interaction with polar water molecules on the wrinkled BN monolayer explains the smaller experimentally measured CAs compared to the computational derived CAs.¹⁷⁹ Based on molecular orbital theory, three hybridized sp^2 orbitals exist for both B and N due to the combination of one $2s$ -orbital with two $2p$ -orbitals ($2p_x$ and $2p_y$). These planar σ bonds are formed around each atom. Due to the different electronegativities of B and N, charge transfer along the sp^2 – σ bonds takes place, which results in polar B–N bonds, as illustrated in Fig. 20(a). However, owing to the hexagonal structural symmetry, the overall dipole moment of the surface in the x and y directions is zero. On the other hand, a non-hybridized p_z atomic orbital remains on each component, which is perpendicular to the plane of the three sp^2 orbitals. In N, two electrons with opposite spins are assumed to occupy $p_{z(N)}$, but in B, $p_{z(B)}$ remains empty. Thus, the two $p_{z(N)}$ electrons might be available, in part, for π -bonding *via* the partial transfer of electrons from $p_{z(N)}$ to $p_{z(B)}$. This does not compensate for the charge transfer along the sp^2 – σ bonds from B to N, but can cause finite interactions of p_z orbitals in succeeding atomic sheets in multilayered BN, as shown in Fig. 20(b).¹¹⁶ Simulation shows that since the upper p_z orbitals in the foremost layer do not interact with any other p_z orbitals, limited dipole moments can exist in the z direction, normal to the atomic plane of BN (Fig. 20(c)). However, when wrinkles exist, the dipole moments on the surface

significantly increase due to the contribution of the B–N bonds that are not parallel to the xy plane in the wrinkled structure. In fact, the σ -related dipole moment components in the z direction can intensify the overall dipole moment on the surface (Fig. 20(d)).¹¹⁶ This can greatly intensify the wettability of the surface.¹⁸⁰

In the case of vertically standing BN nanosheets, a composite (BN/air) structure interfaces with a water droplet and the fraction of BN in contact with the liquid is very limited. Thus, the overall interaction of BN dipole moments and water molecules is small. Instead, the interaction of water molecules with themselves and the surrounding atmosphere (air) becomes crucial in determining the final shape of the droplet on the surface. Since the surface tension of the water droplet gives it a near-spherical shape, and considering the limited interaction of the droplet with the edges of the vertically standing BN nanosheets, the droplet keeps its near-spherical shape, giving superhydrophobic features to the surface.¹¹⁶ Such BN nanostructure films are anticipated to find industrial applications in water-repelling, anti-fouling, self-cleaning, and anti-corrosion systems.

4.6 Other properties and applications

4.6.1 Piezoelectricity. The symmetry properties of BN monolayers endow them with piezoelectric properties, whereas the bulk parent crystal of stacked BN layers is not piezoelectric. This suggests potential for unusual electromechanical properties in the few-layered regime. It has been suggested that a BN

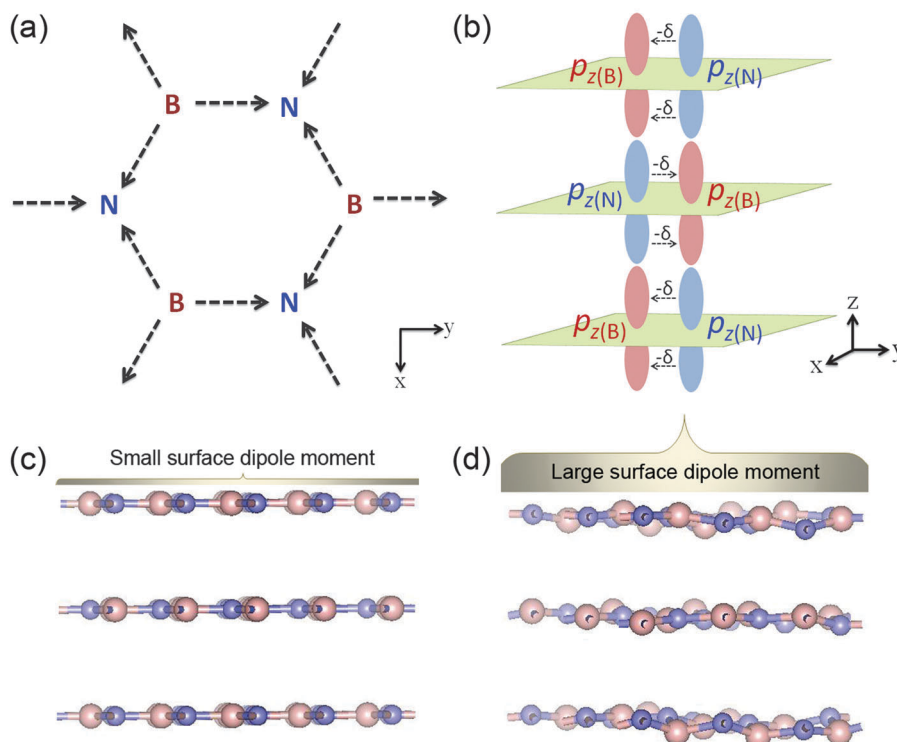


Fig. 20 (a) Charge transfer along the $\text{sp}^2\text{-}\sigma$ bonds in BN. (b) Limited sharing of nitrogen $p_{z(\text{N})}$ electron pair with boron $p_{z(\text{B})}$ (partially available for π -bonding). (c) Limited surface dipole moments in atomically flat BN sheets. (d) Increased surface dipole moments in simulated wrinkled BN sheets.¹¹⁶

bilayer exhibits a strong mechanical coupling between curvature and electric fields, which amplifies its in-plane piezoelectric displacements by exceedingly large factors on the order of $10^3\text{--}10^4$.¹⁸¹ This type of electromechanical coupling is an emergent nanoscale property making such BN-based piezoelectric components an essential feature of modern low-power, high-precision technology.

4.6.2 Field emission. Vertically aligned BN nanosheets can be suitable choices for field emission applications, since their sharp edges can serve as efficient electron emitting sites. Highly porous BN nanospheres consisting of open BN nanocones and corrugated BN ribbons have shown stable field emission properties at low turn-on voltages (*e.g.* 1–1.3 V μm^{-1}).¹⁸² The outstanding electron emission properties were attributed to the presence of finite BN ribbons located at the surface of the nanospheres (exhibiting zigzag edges), which behave like metals as confirmed by first-principles calculations.¹⁸² In a similar way, BN nanosheets protruding from Si_3N_4 nanowires and BN microfibers have demonstrated low turn-on voltages of 4.2 and 1.9 V μm^{-1} , respectively, and excellent long-term stability.^{183,184} Such composite nanostructures can find applications in field-emission displays and vacuum microelectronic devices.

4.6.3 Magnetism. Investigations on the magnetic properties of 2D BN nanostructures have mostly focused on BN nanoribbons due to their enhanced quantum confinement from the edge effect with anisotropic magnetic properties that are not present in nanosheets of large lateral sizes.⁴² While zigzag BN nanoribbons have been found to be magnetic

semiconductors with spin-polarized states localized along the edges, they may be turned into half-metals *via* a directional external electric field.^{185,186} DFT calculations on the decoration of BN sheets with H and F predict that BN sheets can become ferromagnetic, antiferromagnetic, or magnetically degenerate depending on how the surface is functionalized. Also, the stability of magnetic coupling of functionalized BN sheet can be further modulated by applying external strain.¹⁸⁷

Moreover, the magnetic properties of 2D BN nanostructures can be modulated by introducing structural defects. Theoretical studies suggest that adatoms or vacancy defects induce magnetic properties in BN monolayers.^{188,189} It has been observed that N vacancy defects have no influence on the magnetic properties, whereas B vacancy defects cause spin polarization in the nearest three N atoms. DFT calculations demonstrate that N-terminated nanodots and antidots in BN monolayer sheets show strong spin anisotropy around the Fermi level (*i.e.*, half-metallicity), whereas B-terminated nanodots lack magnetism due to edge reconstruction.¹⁹⁰ The substitution of C for B and N atoms is relatively facile at the zigzag edges of BN nanoribbons, and these defects can induce spontaneous magnetization and manipulate the magnetic properties of BN nanoribbons.¹⁹¹ Recently, magnetic h-BN hybrid platelets decorated with iron oxide (Fe_3O_4) nanoparticles offered a new strategy for manipulating the anisotropic properties of direction-dependent materials through magnetic alignments.¹⁹² The hybrid sheets were randomly dispersed in an epoxy matrix and were re-oriented in a direction perpendicular to the

substrate under a magnetic field to improve the directional properties of the composite (*e.g.* thermal conductivity).

4.6.4 Catalysis. Recent studies suggest that BN sheets can serve as a unique substrate for catalytic and sensing applications. It is commonly believed that the pristine defect-free BN surface is an inert support for metal particles. However, DFT calculations demonstrate that while Au particles interact weakly with the regular defect-free BN surface, this weak interaction can lead to strong promotion of binding and catalytic activation of O₂ adsorbed on Au/BN.¹⁹³ This effect occurs due to the mixing of Au-5d orbitals with N-p_z orbitals. Although the defect-free BN surface does not act as a good electron donor for the supported O₂-Au, it promotes an electron transfer from Au to O₂, pushing electrons from the gold to adsorbed oxygen. In the case of the defected h-BN surface, Au can be trapped effectively by N or B vacancies and impurity point defects. Strong adsorption on the surface defects is accompanied by large charge transfer to/from the adsorbate. The excess of positive or negative charge on the supported Au can considerably promote its catalytic activity.¹⁹³ Experimental studies on monodispersed Pt and Au nanoparticles on BN nanosheets also indicate that Au/BN and Pt/BN can be efficient catalysts in various reactions. For instance, the Pt/BN nanosheet catalysts have shown a lower full CO conversion temperature and higher stability, compared to previous reports on many other substrates (*e.g.* Al₂O₃, CeO₂).¹²¹ Another example is Ag nanoparticle-decorated BN nanosheets produced by chemical reduction of an Ag salt with hydrazine in the presence of BN nanosheets. The resultant Ag-BN nanohybrids were transferred onto quartz substrates forming thin film coatings, and were tested as reusable surface-enhanced Raman spectroscopy (SERS) sensors which were robust against repeated solvent washing. In addition, because of the unique thermal oxidation-resistant properties of the BN nanosheets, the sensor devices may be readily recycled by using short-duration high temperature air oxidation to remove residual analyte molecules in repeated runs.¹⁹⁴

4.6.5 Ecology and biology. Layered materials, such as BN, have not only proven to be of technological importance in a variety of industrial applications, but also they are critical to a number of environmental issues involving the fate of contaminants and ground water quality. Very recently, porous BN nanosheets with high specific surface areas exhibited excellent sorption performances for a wide range of oils, solvents and dyes, and were proved to be effective for the removal of such contaminations from water.¹⁹⁵

Moreover, considering the relatively flexible interlayer space in layered nanomaterials, 2D BN nanostructures may be able to accommodate various sized molecules such as proteins, viruses, pesticides, *etc.* Therefore, BN nanosheets may find ecological and biological applications, provided that extensive research on the biocompatibility and toxicity levels of these layered nanomaterials is performed. A recent study suggests that if layered materials (including BN) are functionalized with bioactive molecules, they can be stabilized as uniformly dispersed suspensions with biocompatibility factored in.¹⁹⁶

Such functionalized hybrid nanosheets offer scope for applications in biomedical fields, and beyond.

5. Summary and perspectives

Recent rapid progress in the basic science and applications of layered nanomaterials such as h-BN has been accompanied by an explosion of interest in their 2D nanostructures. These ultrathin nanostructures combine excellent mechanical strength, high thermal conductivity, and exceptional chemical and thermal stabilities, as well as many other interesting properties, which make them highly attractive for applications in different fields of science and technology. In this review, we have discussed the evolution of research on 2D BN nanostructures in terms of synthesis, structural analysis, properties, and prospective applications.

Among the allotropes of BN, the hexagonal form is a layered structure serving as the parent material for BN nanostructures, such as BN monolayers, nanosheets, nanoribbons and nanomeshes. An h-BN layer is isostructural to graphene, with alternating B and N atoms forming the hexagonal rings. However, topological defects can locally change the hexagonal structure by forming square-octagon (4-8) or pentagon-heptagon (5-7) rings, as predicted in theory and confirmed in high-resolution TEM studies. Other defects, such as vacancies, adatoms, and grain boundaries can also locally distort the planar sp² structure of the BN layers.

A variety of methods have been used to synthesize 2D BN nanostructures, such as mechanical and chemical exfoliations, solid-state and substitution reactions, CVD, high-energy electron irradiation, and unzipping of BN nanotubes. However, there is still a long way to go to improve the current yield of the products, especially in the case of BN nanoribbons. The envisaged market for 2D BN nanomaterials applications is essentially dependent on progress in the production of nanosheets and nanoribbons with controlled size, edge structure, and layer number, which is likely to remain a major challenge for the next decade.

2D BN nanostructures are a matter of interest due to their high thermal conductivity, superb oxidation resistance, excellent chemical and thermal stability, electrical insulation, and mechanical robustness. This unique combination of properties promotes their usage in various applications such as multi-functional fillers in composite materials, thermally robust catalytic and sensing substrates, highly durable field emitters, compact UV laser devices, and chemically inert superhydrophobic films. Also, it has been recently shown that BN nanosheets can be a promising “green” lubricant additive for water,¹⁹⁷ and BN sheet-polymer hybrid films can be a suitable choice for marine corrosion protective coatings.¹⁹⁸

Being structurally related to graphene but having its own distinctive properties, 2D BN offers the possibility of fine-tuning characteristics in combination with graphene.^{199,200} For instance, 2D heterostructures based on a BN substrate (as an improved dielectric for graphene devices) exhibit enhanced carrier mobility, and may also have a widened band gap.

In addition, BN-C hybrid nanosheets have great potential for applications in electronic devices with controlled band gaps, fuel cells and transistors. In fact, as a member of the diverse family of 2D crystals and heterostructures, BN layers have great chances of commercial success in the near future.

Acknowledgements

The authors would like to thank the World Premier International Center for Materials Nanoarchitectonics (WPI-MANA) of the National Institute for Materials Science (NIMS; Tsukuba, Japan) for the financial support, and Drs Chunyi Zhi, Masanori Mitome, Naoyuki Kawamoto, and Xuebing Wang for their technical assistance. D.G. acknowledges a “Mega-Grant” award for leading scientists tenable at the National University of Science and Technology “MISIS”, Moscow, Russian Federation, under the agreement No. 11.G34.31.0061.

Notes and references

- 1 W. H. Balmain, *Philos. Mag. Series 3*, 1842, **21**, 270–277.
- 2 W. H. Balmain, *J. Prakt. Chem.*, 1842, **27**, 422–430.
- 3 A. Sokolowska and M. Wronikowski, *J. Cryst. Growth*, 1986, **76**, 511–513.
- 4 V. L. Solozhenko, V. Z. Turkevich and W. B. Holzapfel, *J. Phys. Chem. B*, 1999, **103**, 2903–2905.
- 5 G. Will, G. Nover and J. von der Gonna, *J. Solid State Chem.*, 2000, **154**, 280–285.
- 6 J. Furthmuller, J. Hafner and G. Kresse, *Phys. Rev. B: Condens. Matter*, 1994, **50**, 15606–15622.
- 7 K. Albe, *Phys. Rev. B: Condens. Matter*, 1997, **55**, 6203–6210.
- 8 G. Kern, G. Kresse and J. Hafner, *Phys. Rev. B: Condens. Matter*, 1999, **59**, 8551–8559.
- 9 T. E. Mosuang and J. E. Lowther, *J. Phys. Chem. Solids*, 2002, **63**, 363–368.
- 10 W. J. Yu, W. M. Lau, S. P. Chan, Z. F. Liu and Q. Q. Zheng, *Phys. Rev. B: Condens. Matter*, 2003, **67**, 014108.
- 11 M. Topsakal, E. Akturk and S. Ciraci, *Phys. Rev. B: Condens. Matter Mater. Phys.*, 2009, **79**, 115442.
- 12 R. Ahmed, Fazal-e-Aleem, S. J. Hashemifar and H. Akbarzadeh, *Phys. B*, 2007, **400**, 297–306.
- 13 Y. N. Xu and W. Y. Ching, *Phys. Rev. B: Condens. Matter*, 1991, **44**, 7787–7798.
- 14 M. Halo, C. Pisani, L. Maschio, S. Casassa, M. Schutz and D. Usuyat, *Phys. Rev. B: Condens. Matter Mater. Phys.*, 2011, **83**, 035117.
- 15 A. Oberlin, M. Endo and T. Koyama, *J. Cryst. Growth*, 1976, **32**, 335–349.
- 16 N. G. Chopra, R. J. Luyken, K. Cherrey, V. H. Crespi, M. L. Cohen, S. G. Louie and A. Zettl, *Science*, 1995, **269**, 966–967.
- 17 J. C. Yong, Z. Z. Hong and C. Ying, *Nanotechnology*, 2006, **17**, 786–789.
- 18 Y. J. Qiu, J. Yu, J. Yin, C. L. Tan, X. S. Zhou, X. D. Bai and E. G. Wang, *Nanotechnology*, 2009, **20**, 345603.
- 19 H. Z. Zhang, J. Yu, Y. Chen and J. FitzGerald, *J. Am. Ceram. Soc.*, 2006, **89**, 675–679.
- 20 H. W. Kroto, J. R. Heath, S. C. O'Brien, R. F. Curl and R. E. Smalley, *Nature*, 1985, **318**, 162–163.
- 21 O. Stephan, Y. Bando, A. Loiseau, F. Willaime, N. Shramchenko, T. Tamiya and T. Sato, *Appl. Phys. A: Mater. Sci. Process.*, 1998, **67**, 107–111.
- 22 D. Golberg, Y. Bando, O. Stephan and K. Kurashima, *Appl. Phys. Lett.*, 1998, **73**, 2441–2443.
- 23 K. S. Novoselov, A. K. Geim, S. V. Morozov, D. Jiang, Y. Zhang, S. V. Dubonos, I. V. Grigorieva and A. A. Firsov, *Science*, 2004, **306**, 666–669.
- 24 D. Golberg, Y. Bando, Y. Huang, T. Terao, M. Mitome, C. C. Tang and C. Y. Zhi, *ACS Nano*, 2010, **4**, 2979–2993.
- 25 M. Corso, W. Auwarter, M. Muntwiler, A. Tamai, T. Greber and J. Osterwalder, *Science*, 2004, **303**, 217–220.
- 26 K. S. Novoselov, D. Jiang, F. Schedin, T. J. Booth, V. V. Khotkevich, S. V. Morozov and A. K. Geim, *Proc. Natl. Acad. Sci. U. S. A.*, 2005, **102**, 10451–10453.
- 27 Z. G. Chen, J. Zou, G. Liu, F. Li, Y. Wang, L. Z. Wang, X. L. Yuan, T. Sekiguchi, H. M. Cheng and G. Q. Lu, *ACS Nano*, 2008, **2**, 2183–2191.
- 28 L. Pauling, *Proc. Natl. Acad. Sci. U. S. A.*, 1966, **56**, 1646–1652.
- 29 C. Y. Zhi, Y. Bando, C. C. Tang, H. Kuwahara and D. Golberg, *Adv. Mater.*, 2009, **21**, 2889–2893.
- 30 X. Blase, A. De Vita, J. C. Charlier and R. Car, *Phys. Rev. Lett.*, 1998, **80**, 1666–1669.
- 31 J. C. Charlier, X. Blase, A. De Vita and R. Car, *Appl. Phys. A: Mater. Sci. Process.*, 1999, **68**, 267–273.
- 32 D. Golberg and Y. Bando, *Appl. Phys. Lett.*, 2001, **79**, 415–417.
- 33 M. B. Nardelli, C. Brabec, A. Maiti, C. Roland and J. Bernholc, *Phys. Rev. Lett.*, 1998, **80**, 313–316.
- 34 N. Alem, Q. M. Ramasse, C. R. Seabourne, O. V. Yazev, K. Erickson, M. C. Sarahan, C. Kisielowski, A. J. Scott, S. G. Louie and A. Zettl, *Phys. Rev. Lett.*, 2012, **109**, 205502.
- 35 N. Marom, J. Bernstein, J. Garel, A. Tkatchenko, E. Joselevich, L. Kronik and O. Hod, *Phys. Rev. Lett.*, 2010, **105**, 046801.
- 36 A. Pakdel, Y. Bando, D. Shtansky and D. Golberg, *Surface Innovations*, 2013, **1**, 32–39.
- 37 X. B. Wang, A. Pakdel, C. Y. Zhi, K. Watanabe, T. Sekiguchi, D. Golberg and Y. Bando, *J. Phys.: Condens. Matter*, 2012, **24**, 314205.
- 38 M. Mitome, H. Sawada, Y. Kondo, Y. Tanishiro and K. Takayanagi, *Ultramicroscopy*, 2012, **122**, 6–11.
- 39 L. Qin, J. Yu, M. Y. Li, F. Liu and X. D. Bai, *Nanotechnology*, 2011, **22**, 215602.
- 40 F. Banhart, J. Kotakoski and A. V. Krasheninnikov, *ACS Nano*, 2011, **5**, 26–41.
- 41 W. Chen, Y. F. Li, G. T. Yu, Z. Zhou and Z. F. Chen, *J. Chem. Theory Comput.*, 2009, **5**, 3088–3095.
- 42 Y. Lin and J. W. Connell, *Nanoscale*, 2012, **4**, 6908–6939.
- 43 P. Y. Huang, C. S. Ruiz-Vargas, A. M. van der Zande, W. S. Whitney, M. P. Levendorf, J. W. Kevek, S. Garg,

- J. S. Alden, C. J. Hustedt, Y. Zhu, J. Park, P. L. McEuen and D. A. Muller, *Nature*, 2011, **469**, 389–392.
- 44 K. Kim, Z. Lee, W. Regan, C. Kisielowski, M. F. Crommie and A. Zettl, *ACS Nano*, 2011, **5**, 2142–2146.
- 45 O. V. Yazyev and S. G. Louie, *Nat. Mater.*, 2010, **9**, 806–809.
- 46 J. F. Zhang, J. J. Zhao and J. P. Lu, *ACS Nano*, 2012, **6**, 2704–2711.
- 47 Y. J. Wei, J. T. Wu, H. Q. Yin, X. H. Shi, R. G. Yang and M. Dresselhaus, *Nat. Mater.*, 2012, **11**, 759–763.
- 48 D. Gunlycke and C. T. White, *Phys. Rev. Lett.*, 2011, **106**, 136806.
- 49 Y. Y. Liu, X. L. Zou and B. I. Yakobson, *ACS Nano*, 2012, **6**, 7053–7058.
- 50 A. L. Gibb, N. Alem, J.-H. Chen, K. J. Erickson, J. Ciston, A. Gautam, M. Linck and A. Zettl, *J. Am. Chem. Soc.*, 2013, **135**, 6758–6761.
- 51 E. Bengu and L. D. Marks, *Phys. Rev. Lett.*, 2001, **86**, 2385–2387.
- 52 C. H. Jin, F. Lin, K. Suenaga and S. Iijima, *Phys. Rev. Lett.*, 2009, **102**, 195505.
- 53 J. C. Meyer, A. Chuwilin, G. Algara-Siller, J. Biskupek and U. Kaiser, *Nano Lett.*, 2009, **9**, 2683–2689.
- 54 N. Alem, R. Erni, C. Kisielowski, M. D. Rossell, W. Gannett and A. Zettl, *Phys. Rev. B: Condens. Matter Mater. Phys.*, 2009, **80**, 155425.
- 55 A. Zobelli, A. Gloter, C. P. Ewels, G. Seifert and C. Colliex, *Phys. Rev. B: Condens. Matter Mater. Phys.*, 2007, **75**, 245402.
- 56 D. Pacile, J. C. Meyer, C. O. Girit and A. Zettl, *Appl. Phys. Lett.*, 2008, **92**, 133107.
- 57 R. V. Gorbachev, I. Riaz, R. R. Nair, R. Jalil, L. Britnell, B. D. Belle, E. W. Hill, K. S. Novoselov, K. Watanabe, T. Taniguchi, A. K. Geim and P. Blake, *Small*, 2011, **7**, 465–468.
- 58 A. Pakdel, C. Y. Zhi, Y. Bando and D. Golberg, *Mater. Today*, 2012, **15**, 256–265.
- 59 L. H. Li, Y. Chen, G. Behan, H. Z. Zhang, M. Petracic and A. M. Glushenkova, *J. Mater. Chem.*, 2011, **21**, 11862–11866.
- 60 W. Q. Han, L. J. Wu, Y. M. Zhu, K. Watanabe and T. Taniguchi, *Appl. Phys. Lett.*, 2008, **93**, 223103.
- 61 J. H. Warner, M. H. Rummeli, A. Bachmatiuk and B. Buchner, *ACS Nano*, 2010, **4**, 1299–1304.
- 62 Y. Lin, T. V. Williams and J. W. Connell, *J. Phys. Chem. Lett.*, 2010, **1**, 277–283.
- 63 Y. Wang, Z. X. Shi and J. Yin, *J. Mater. Chem.*, 2011, **21**, 11371–11377.
- 64 X. Li, X. Hao, M. Zhao, Y. Wu, J. Yang, Y. Tian and G. Qian, *Adv. Mater.*, 2013, **25**, 2200–2204.
- 65 H. Yurdakul, Y. Göncü, O. Durukan, A. Akay, A. T. Seyhan, N. Ay and S. Turan, *Ceram. Int.*, 2012, **38**, 2187–2193.
- 66 X. J. Chen, J. F. Dobson and C. L. Raston, *Chem. Commun.*, 2012, **48**, 3703–3705.
- 67 M. Basche, *U.S. Pat.*, 3, 152, 006, 1964.
- 68 M. J. Rand and J. F. Roberts, *J. Electrochem. Soc.*, 1968, **115**, 423–429.
- 69 H. O. Pierson, *J. Compos. Mater.*, 1975, **9**, 228–240.
- 70 A. S. Rozenberg, Y. A. Sinenko and N. V. Chukanov, *J. Mater. Sci.*, 1993, **28**, 5528–5533.
- 71 S. Middleman, *Mater. Sci. Eng., A*, 1993, **163**, 135–140.
- 72 A. C. Adams, *J. Electrochem. Soc.*, 1981, **128**, 1378–1379.
- 73 W. Auwarter, H. U. Suter, H. Sachdev and T. Greber, *Chem. Mater.*, 2004, **16**, 343–345.
- 74 F. Muller, K. Stowe and H. Sachdev, *Chem. Mater.*, 2005, **17**, 3464–3467.
- 75 G. Constant and R. Feurer, *J. Less Common Met.*, 1981, **82**, 113–118.
- 76 M. T. Paffett, R. J. Simonson, P. Papin and R. T. Paine, *Surf. Sci.*, 1990, **232**, 286–296.
- 77 H. O. Pierson, *J. Compos. Mater.*, 1975, **9**, 228–240.
- 78 N. J. Archer, *Phys. Technol.*, 1979, **10**, 152–161.
- 79 Y. Gamou, M. Terai, A. Nagashima and C. Oshima, *Sci. Rep. Res. Inst., Tohoku Univ., Ser. A*, 1997, **44**, 211–214.
- 80 W. Auwarter, T. J. Kreutz, T. Greber and J. Osterwalder, *Surf. Sci.*, 1999, **429**, 229–236.
- 81 G. B. Grad, P. Blaha, K. Schwarz, W. Auwarter and T. Greber, *Phys. Rev. B: Condens. Matter*, 2003, **68**, 085404.
- 82 M. N. Huda and L. Kleinman, *Phys. Rev. B: Condens. Matter Mater. Phys.*, 2006, **74**, 075418.
- 83 E. Cavar, R. Westerstrom, A. Mikkelsen, E. Lundgren, A. S. Vinogradov, M. L. Ng, A. B. Preobrajenski, A. A. Zakharov and N. Martensson, *Surf. Sci.*, 2008, **602**, 1722–1726.
- 84 R. Laskowski, P. Blaha and K. Schwarz, *Phys. Rev. B: Condens. Matter Mater. Phys.*, 2008, **78**, 045409.
- 85 M. Morscher, M. Corso, T. Greber and J. Osterwalder, *Surf. Sci.*, 2006, **600**, 3280–3284.
- 86 A. Goriachko, Y. B. He, M. Knapp, H. Over, M. Corso, T. Brugger, S. Berner, J. Osterwalder and T. Greber, *Langmuir*, 2007, **23**, 2928–2931.
- 87 A. Nagashima, N. Tejima, Y. Gamou, T. Kawai and C. Oshima, *Phys. Rev. B: Condens. Matter*, 1995, **51**, 4606–4613.
- 88 E. Rokuta, Y. Hasegawa, K. Suzuki, Y. Gamou, C. Oshima and A. Nagashima, *Phys. Rev. Lett.*, 1997, **79**, 4609–4612.
- 89 M. Muntwiler, W. Auwarter, F. Baumberger, M. Hoesch, T. Greber and J. Osterwalder, *Surf. Sci.*, 2001, **472**, 125–132.
- 90 A. B. Preobrajenski, A. S. Vinogradov and N. Mårtensson, *Phys. Rev. B: Condens. Matter Mater. Phys.*, 2004, **70**, 165404.
- 91 A. B. Preobrajenski, A. S. Vinogradov and N. Martensson, *Surf. Sci.*, 2005, **582**, 21–30.
- 92 A. B. Preobrajenski, A. S. Vinogradov, M. L. Ng, E. Ćavar, R. Westerström, A. Mikkelsen, E. Lundgren and N. Mårtensson, *Phys. Rev. B: Condens. Matter Mater. Phys.*, 2007, **75**, 245412.
- 93 M. Morscher, M. Corso, T. Greber and J. Osterwalder, *Surf. Sci.*, 2006, **600**, 3280–3284.
- 94 M. Corso, T. Greber and J. Osterwalder, *Surf. Sci.*, 2005, **577**, L78–L84.
- 95 N. A. Vinogradov, A. A. Zakharov, M. L. Ng, A. Mikkelsen, E. Lundgren, N. Martensson and A. B. Preobrajenski, *Langmuir*, 2012, **28**, 1775–1781.
- 96 M. P. Allan, S. Berner, M. Corso, T. Greber and J. Osterwalder, *Nanoscale Res. Lett.*, 2007, **2**, 94–99.
- 97 F. Müller, S. Hüfner and H. Sachdev, *Surf. Sci.*, 2008, **602**, 3467–3476.

- 98 S. Joshi, D. Ecija, R. Koitz, M. Iannuzzi, A. P. Seitsonen, J. Hutter, H. Sachdev, S. Vijayaraghavan, F. Bischoff, K. Seufert, J. V. Barth and W. Auwarter, *Nano Lett.*, 2012, **12**, 5821–5828.
- 99 K. K. Kim, A. Hsu, X. T. Jia, S. M. Kim, Y. S. Shi, M. Hofmann, D. Nezich, J. F. Rodriguez-Nieva, M. Dresselhaus, T. Palacios and J. Kong, *Nano Lett.*, 2012, **12**, 161–166.
- 100 Q. K. Yu, L. A. Jauregui, W. Wu, R. Colby, J. F. Tian, Z. H. Su, H. L. Cao, Z. H. Liu, D. Pandey, D. G. Wei, T. F. Chung, P. Peng, N. P. Guisinger, E. A. Stach, J. M. Bao, S. S. Pei and Y. P. Chen, *Nat. Mater.*, 2011, **10**, 443–449.
- 101 P. Sutter, J. Lahiri, P. Albrecht and E. Sutter, *ACS Nano*, 2011, **5**, 7303–7309.
- 102 S. Berner, M. Corso, R. Widmer, O. Groening, R. Laskowski, P. Blaha, K. Schwarz, A. Goriachko, H. Over, S. Gsell, M. Schreck, H. Sachdev, T. Greber and J. Osterwalder, *Angew. Chem., Int. Ed.*, 2007, **46**, 5115–5119.
- 103 O. Bunk, M. Corso, D. Martoccia, R. Herger, P. R. Willmott, B. D. Patterson, J. Osterwalder, I. van der Veen and T. Greber, *Surf. Sci.*, 2007, **601**, L7–L10.
- 104 R. Laskowski, P. Blaha, T. Gallauer and K. Schwarz, *Phys. Rev. Lett.*, 2007, **98**, 106802.
- 105 D. Martoccia, T. Brugger, M. Bjorck, C. M. Schleputz, S. A. Pauli, T. Greber, B. D. Patterson and P. R. Willmott, *Surf. Sci.*, 2010, **604**, L16–L19.
- 106 L. Song, L. J. Ci, H. Lu, P. B. Sorokin, C. H. Jin, J. Ni, A. G. Kvashnin, D. G. Kvashnin, J. Lou, B. I. Yakobson and P. M. Ajayan, *Nano Lett.*, 2010, **10**, 3209–3215.
- 107 Y. M. Shi, C. Hamsen, X. T. Jia, K. K. Kim, A. Reina, M. Hofmann, A. L. Hsu, K. Zhang, H. N. Li, Z. Y. Juang, M. S. Dresselhaus, L. J. Li and J. Kong, *Nano Lett.*, 2010, **10**, 4134–4139.
- 108 S. Chatterjee, Z. T. Luo, M. Acerce, D. M. Yates, A. T. C. Johnson and L. G. Sneddon, *Chem. Mater.*, 2011, **23**, 4414–4416.
- 109 W. Auwarter, M. Muntwiler, J. Osterwalder and T. Greber, *Surf. Sci.*, 2003, **545**, L735–L740.
- 110 Y. H. Lee, K. K. Liu, A. Y. Lu, C. Y. Wu, C. T. Lin, W. J. Zhang, C. Y. Su, C. L. Hsu, T. W. Lin, K. H. Wei, Y. M. Shi and L. J. Li, *RSC Adv.*, 2012, **2**, 111–115.
- 111 Y. Gao, W. C. Ren, T. Ma, Z. B. Liu, Y. Zhang, W. B. Liu, L. P. Ma, X. L. Ma and H. M. Cheng, *ACS Nano*, 2013, **7**, 5199–5206.
- 112 R. Gao, L. W. Yin, C. X. Wang, Y. X. Qi, N. Lun, L. Y. Zhang, Y. X. Liu, L. Kang and X. F. Wang, *J. Phys. Chem. C*, 2009, **113**, 15160–15165.
- 113 A. Nag, K. Raidongia, K. P. S. S. Hembram, R. Datta, U. V. Waghmare and C. N. R. Rao, *ACS Nano*, 2010, **4**, 1539–1544.
- 114 J. Yu, L. Qin, Y. F. Hao, S. Kuang, X. D. Bai, Y. M. Chong, W. J. Zhang and E. Wang, *ACS Nano*, 2010, **4**, 414–422.
- 115 A. Pakdel, C. Y. Zhi, Y. Bando, T. Nakayama and D. Golberg, *ACS Nano*, 2011, **5**, 6507–6515.
- 116 A. Pakdel, X. B. Wang, Y. Bando and D. Golberg, *Acta Mater.*, 2013, **61**, 1266–1273.
- 117 G. Lian, X. Zhang, M. Tan, S. J. Zhang, D. L. Cui and Q. L. Wang, *J. Mater. Chem.*, 2011, **21**, 9201–9207.
- 118 S. Zhang, G. Lian, H. Si, J. Wang, X. Zhang, Q. Wang and D. Cui, *J. Mater. Chem. A*, 2013, **1**, 5105–5112.
- 119 X. B. Wang, C. Y. Zhi, L. Li, H. B. Zeng, C. Li, M. Mitome, D. Golberg and Y. Bando, *Adv. Mater.*, 2011, **23**, 4072–4076.
- 120 Z. Y. Zhao, Z. G. Yang, Y. Wen and Y. H. Wang, *J. Am. Ceram. Soc.*, 2011, **94**, 4496–4501.
- 121 L. C. Wang, C. H. Sun, L. Q. Xu and Y. T. Qian, *Catal. Sci. Technol.*, 2011, **1**, 1119–1123.
- 122 W. Q. Han, H. G. Yu and Z. X. Liu, *Appl. Phys. Lett.*, 2011, **98**, 203112.
- 123 L. Y. Jiao, L. Zhang, X. R. Wang, G. Diankov and H. J. Dai, *Nature*, 2009, **458**, 877–880.
- 124 H. B. Zeng, C. Y. Zhi, Z. H. Zhang, X. L. Wei, X. B. Wang, W. L. Guo, Y. Bando and D. Golberg, *Nano Lett.*, 2010, **10**, 5049–5055.
- 125 K. J. Erickson, A. L. Gibb, A. Sinitskii, M. Rousseas, N. Alem, J. M. Tour and A. K. Zettl, *Nano Lett.*, 2011, **11**, 3221–3226.
- 126 S. Okada and M. Otani, *Phys. Rev. B: Condens. Matter Mater. Phys.*, 2010, **81**, 233401.
- 127 D. V. Kosynkin, W. Lu, A. Sinitskii, G. Pera, Z. Z. Sun and J. M. Tour, *ACS Nano*, 2011, **5**, 968–974.
- 128 R. Arenal, X. Blase and A. Loiseau, *Adv. Phys.*, 2010, **59**, 101–179.
- 129 C. R. Dean, A. F. Young, I. Meric, C. Lee, L. Wang, S. Sorgenfrei, K. Watanabe, T. Taniguchi, P. Kim, K. L. Shepard and J. Hone, *Nat. Nanotechnol.*, 2010, **5**, 722–726.
- 130 J. M. Xue, J. Sanchez-Yamagishi, D. Bulmash, P. Jacquod, A. Deshpande, K. Watanabe, T. Taniguchi, P. Jarillo-Herrero and B. J. Leroy, *Nat. Mater.*, 2011, **10**, 282–285.
- 131 R. Decker, Y. Wang, V. W. Brar, W. Regan, H. Z. Tsai, Q. Wu, W. Gannett, A. Zettl and M. F. Crommie, *Nano Lett.*, 2011, **11**, 2291–2295.
- 132 A. S. Mayorov, R. V. Gorbachev, S. V. Morozov, L. Britnell, R. Jalil, L. A. Ponomarenko, P. Blake, K. S. Novoselov, K. Watanabe, T. Taniguchi and A. K. Geim, *Nano Lett.*, 2011, **11**, 2396–2399.
- 133 G. H. Lee, Y. J. Yu, C. Lee, C. Dean, K. L. Shepard, P. Kim and J. Hone, *Appl. Phys. Lett.*, 2011, **99**, 243114.
- 134 L. Britnell, R. V. Gorbachev, R. Jalil, B. D. Belle, F. Schedin, A. Mishchenko, T. Georgiou, M. I. Katsnelson, L. Eaves, S. V. Morozov, N. M. R. Peres, J. Leist, A. K. Geim, K. S. Novoselov and L. A. Ponomarenko, *Science*, 2012, **335**, 947–950.
- 135 L. Britnell, R. V. Gorbachev, R. Jalil, B. D. Belle, F. Schedin, M. I. Katsnelson, L. Eaves, S. V. Morozov, A. S. Mayorov, N. M. R. Peres, A. H. C. Neto, J. Leist, A. K. Geim, L. A. Ponomarenko and K. S. Novoselov, *Nano Lett.*, 2012, **12**, 1707–1710.
- 136 F. Amet, J. R. Williams, A. G. F. Garcia, M. Yankowitz, K. Watanabe, T. Taniguchi and D. Goldhaber-Gordon, *Phys. Rev. B: Condens. Matter Mater. Phys.*, 2012, **85**, 073405.

- 137 A. J. Du, S. C. Smith and G. Q. Lu, *Chem. Phys. Lett.*, 2007, **447**, 181–186.
- 138 Z. Zhang and W. Guo, *Phys. Rev. B: Condens. Matter Mater. Phys.*, 2008, **77**, 075403.
- 139 C. H. Park and S. G. Louie, *Nano Lett.*, 2008, **8**, 2200–2203.
- 140 H. X. Zhang and P. X. Feng, *ACS Appl. Mater. Interfaces*, 2012, **4**, 30–33.
- 141 D. K. Samarakoon and X. Q. Wang, *Appl. Phys. Lett.*, 2012, **100**, 103107.
- 142 W. Chen, Y. F. Li, G. T. Yu, C. Z. Li, S. B. B. Zhang, Z. Zhou and Z. F. Chen, *J. Am. Chem. Soc.*, 2010, **132**, 1699–1705.
- 143 Y. Ding, Y. L. Wang and J. Ni, *Appl. Phys. Lett.*, 2009, **94**, 233107.
- 144 Y. L. Wang, Y. Ding and J. Ni, *Appl. Phys. Lett.*, 2011, **99**, 053123.
- 145 A. Pakdel, X. B. Wang, C. Y. Zhi, Y. Bando, K. Watanabe, T. Sekiguchi, T. Nakayama and D. Golberg, *J. Mater. Chem.*, 2012, **22**, 4818–4824.
- 146 L. Ci, L. Song, C. H. Jin, D. Jariwala, D. X. Wu, Y. J. Li, A. Srivastava, Z. F. Wang, K. Storr, L. Balicas, F. Liu and P. M. Ajayan, *Nat. Mater.*, 2010, **9**, 430–435.
- 147 L. Qin, J. Yu, S. Y. Kuang, C. Xiao and X. D. Bai, *Nanoscale*, 2012, **4**, 120–123.
- 148 J. N. Coleman, M. Lotya, A. O'Neill, S. D. Bergin, P. J. King, U. Khan, K. Young, A. Gaucher, S. De, R. J. Smith, I. V. Shvets, S. K. Arora, G. Stanton, H. Y. Kim, K. Lee, G. T. Kim, G. S. Duesberg, T. Hallam, J. J. Boland, J. J. Wang, J. F. Donegan, J. C. Grunlan, G. Moriarty, A. Shmeliov, R. J. Nicholls, J. M. Perkins, E. M. Grieveson, K. Theuwissen, D. W. McComb, P. D. Nellist and V. Nicolosi, *Science*, 2011, **331**, 568–571.
- 149 K. Watanabe, T. Taniguchi and H. Kanda, *Nat. Mater.*, 2004, **3**, 404–409.
- 150 P. Jaffrennou, J. Barjon, J. S. Lauret, B. Attal-Tretout, F. Ducastelle and A. Loiseau, *J. Appl. Phys.*, 2007, **102**, 116102.
- 151 M. G. Silly, P. Jaffrennou, J. Barjon, J. S. Lauret, F. Ducastelle, A. Loiseau, E. Obraztsova, B. Attal-Tretout and E. Rosencher, *Phys. Rev. B: Condens. Matter Mater. Phys.*, 2007, **75**, 085205.
- 152 T. Kuzuba, Y. Sato, S. Yamaoka and K. Era, *Phys. Rev. B*, 1978, **18**, 4440–4443.
- 153 E. Borowiak-Palen, T. Pichler, G. G. Fuentes, B. Bendjemil, X. Liu, A. Graff, G. Behr, R. J. Kalenczuk, M. Knupfer and J. Fink, *Chem. Commun.*, 2003, 82–83.
- 154 L. Lindsay and D. A. Broido, *Phys. Rev. B: Condens. Matter Mater. Phys.*, 2011, **84**, 155421.
- 155 C. Sevik, A. Kinaci, J. B. Haskins and T. Cagin, *Phys. Rev. B: Condens. Matter Mater. Phys.*, 2011, **84**, 085409.
- 156 L. Lindsay and D. A. Broido, *Phys. Rev. B: Condens. Matter Mater. Phys.*, 2012, **85**, 035436.
- 157 O. Y. Tao, Y. P. Chen, Y. E. Xie, K. K. Yang, Z. G. Bao and J. X. Zhong, *Nanotechnology*, 2010, **21**, 245701.
- 158 H. B. Cho, Y. Tokoi, S. Tanaka, H. Suematsu, T. Suzuki, W. H. Jiang, K. Niihara and T. Nakayama, *Compos. Sci. Technol.*, 2011, **71**, 1046–1052.
- 159 W. L. Song, P. Wang, L. Cao, A. Anderson, M. J. Meziani, A. J. Farr and Y. P. Sun, *Angew. Chem., Int. Ed.*, 2012, **51**, 6498–6501.
- 160 J. H. Yu, X. Y. Huang, C. Wu, X. F. Wu, G. L. Wang and P. K. Jiang, *Polymer*, 2012, **53**, 471–480.
- 161 X. B. Wang, A. Pakdel, J. Zhang, Q. H. Weng, T. Y. Zhai, C. Y. Zhi, D. Golberg and Y. Bando, *Nanoscale Res. Lett.*, 2012, **7**, 662.
- 162 L. J. Romasanta, M. Hernandez, M. A. Lopez-Manchado and R. Verdejo, *Nanoscale Res. Lett.*, 2011, **6**, 508.
- 163 J. Taha-Tijerina, T. N. Narayanan, G. H. Gao, M. Rohde, D. A. Tsentalovich, M. Pasquali and P. M. Ajayan, *ACS Nano*, 2012, **6**, 1214–1220.
- 164 F. Liu, P. M. Ming and J. Li, *Phys. Rev. B: Condens. Matter Mater. Phys.*, 2007, **76**, 064120.
- 165 K. V. Zakharchenko, M. I. Katsnelson and A. Fasolino, *Phys. Rev. Lett.*, 2009, **102**, 046808.
- 166 E. Konstantinova, S. O. Dantas and P. M. V. B. Barone, *Phys. Rev. B: Condens. Matter Mater. Phys.*, 2006, **74**, 035417.
- 167 C. Lee, X. D. Wei, J. W. Kysar and J. Hone, *Science*, 2008, **321**, 385–388.
- 168 K. N. Kudin, G. E. Scuseria and B. I. Yakobson, *Phys. Rev. B: Condens. Matter*, 2001, **64**, 235406.
- 169 H. Sahin, S. Cahangirov, M. Topsakal, E. Bekaroglu, E. Akturk, R. T. Senger and S. Ciraci, *Phys. Rev. B: Condens. Matter Mater. Phys.*, 2009, **80**, 155453.
- 170 L. Boldrin, F. Scarpa, R. Chowdhury and S. Adhikari, *Nanotechnology*, 2011, **22**, 505702.
- 171 R. C. Andrew, R. E. Mapasha, A. M. Ukpong and N. Chetty, *Phys. Rev. B: Condens. Matter Mater. Phys.*, 2012, **85**, 125428.
- 172 C. Li, Y. Bando, C. Y. Zhi, Y. Huang and D. Golberg, *Nanotechnology*, 2009, **20**, 385707.
- 173 I. Nikiforov, D. M. Tang, X. L. Wei, T. Dumitrica and D. Golberg, *Phys. Rev. Lett.*, 2012, **109**, 025504.
- 174 Z.-Q. Duan, Y.-T. Liu, X.-M. Xie and X.-Y. Ye, *Chin. Chem. Lett.*, 2013, **24**, 17–19.
- 175 C. Yue, W. Liu, L. Zhang, T. Zhang and Y. Chen, *Scr. Mater.*, 2013, **68**, 579–582.
- 176 C. H. Lee, J. Drelich and Y. K. Yap, *Langmuir*, 2009, **25**, 4853–4860.
- 177 L. H. Li and Y. Chen, *Langmuir*, 2010, **26**, 5135–5140.
- 178 A. Pakdel, Y. Bando and D. Golberg, *Langmuir*, 2013, **29**, 7529–7533.
- 179 H. Li and X. C. Zeng, *ACS Nano*, 2012, **6**, 2401–2409.
- 180 N. Giovambattista, P. G. Debenedetti and P. J. Rossky, *J. Phys. Chem. B*, 2007, **111**, 9581–9587.
- 181 K.-A. N. Duerloo and E. J. Reed, *Nano Lett.*, 2013, **13**, 1681–1686.
- 182 M. Terrones, J. C. Charlier, A. Gloter, E. Cruz-Silva, E. Terres, Y. B. Li, A. Vinu, Z. Zanolli, J. M. Dominguez, H. Terrones, Y. Bando and D. Golberg, *Nano Lett.*, 2008, **8**, 1026–1032.
- 183 Y. C. Zhu, Y. Bando, L. W. Yin and D. Golberg, *Nano Lett.*, 2006, **6**, 2982–2986.
- 184 Z. G. Chen and J. Zou, *J. Mater. Chem.*, 2011, **21**, 1191–1195.
- 185 V. Barone and J. E. Peralta, *Nano Lett.*, 2008, **8**, 2210–2214.

- 186 M. H. Wu, Z. H. Zhang and X. C. Zeng, *Appl. Phys. Lett.*, 2010, **97**, 093109.
- 187 J. Zhou, Q. Wang, Q. Sun and P. Jena, *Phys. Rev. B: Condens. Matter Mater. Phys.*, 2010, **81**, 085442.
- 188 M. S. Si and D. S. Xue, *Phys. Rev. B: Condens. Matter Mater. Phys.*, 2007, **75**, 193409.
- 189 J. Yang, D. Kim, J. Hong and X. H. Qian, *Surf. Sci.*, 2010, **604**, 1603–1607.
- 190 A. J. Du, Y. Chen, Z. H. Zhu, R. Amal, G. Q. Lu and S. C. Smith, *J. Am. Chem. Soc.*, 2009, **131**, 17354–17359.
- 191 S. B. Tang and Z. X. Cao, *Comput. Mater. Sci.*, 2010, **48**, 648–654.
- 192 H. S. Lim, J. W. Oh, S. Y. Kim, M.-J. Yoo, S.-D. Park and W. S. Lee, *Chem. Mater.*, 2013, **25**, 3315–3319.
- 193 M. Gao, A. Lyalin and T. Taketsugu, *J. Phys. Chem. C*, 2012, **116**, 9054–9062.
- 194 Y. Lin, C. E. Bunker, K. A. S. Fernando and J. W. Connell, *ACS Appl. Mater. Interfaces*, 2012, **4**, 1110–1117.
- 195 W. Lei, D. Portehault, D. Liu, S. Qin and Y. Chen, *Nat. Commun.*, 2013, **4**, 1777.
- 196 F. Zhang, X. Chen, R. A. Boulos, F. Md Yasin, H. Lu, C. Raston and H. Zhang, *Chem. Commun.*, 2013, **49**, 4845–4847.
- 197 D.-H. Cho, J.-S. Kim, S.-H. Kwon, C. Lee and Y.-Z. Lee, *Wear*, 2013, **302**, 981–986.
- 198 E. Husain, T. N. Narayanan, J. J. Taha-Tijerina, S. Vinod, R. Vajtai and P. M. Ajayan, *ACS Appl. Mater. Interfaces*, 2013, **5**, 4129–4135.
- 199 K. S. Novoselov, V. I. Fal'ko, L. Colombo, P. R. Gellert, M. G. Schwab and K. Kim, *Nature*, 2012, **490**, 192–200.
- 200 S. L. Li, Z. Y. Ren, J. M. Zheng, Y. X. Zhou, Y. Wan and L. Hao, *J. Appl. Phys.*, 2013, **113**, 033703.